Deciphering Stiffness-Driven Changes in Colorectal Cancer by Proteomics

Authors

Charlotte Cresens, Ana Montero-Calle, Guillermo Solís-Fernández, Behrad Shaghaghi, Lotte Gerrits, Samet Aytekin, Paul H. J. Kouwer, Rodrigo Barderas, and Susana Rocha

Correspondence

r.barderasm@isciii.es; susana.rocha@kuleuven.be

Graphical Abstract

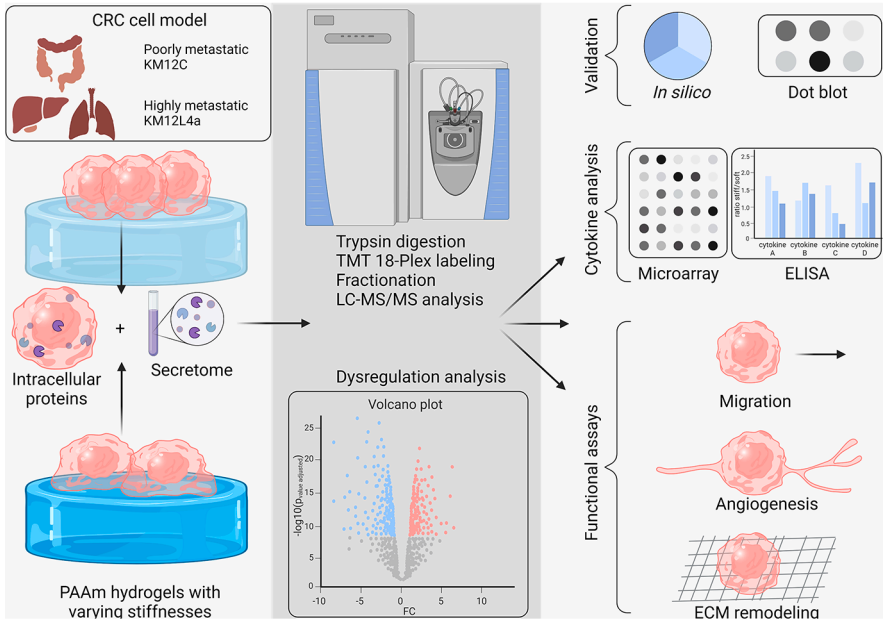

In Brief

This study focused on defining the impact of matrix stiffness on proteome remodeling in colorectal cancer. Deep quantitative proteomics revealed selective reprogramming of the tumor secretome under increased stiffness, whereas the intracellular proteome remained largely unchanged. Label-free quantification identified stiffness-dependent regulation of proteins involved in extracellular matrix organization, angiogenesis, and migration. Functional assays confirmed that these secretome alterations promote protumorigenic phenotypes, highlighting matrix stiffness as a regulator of extracellular dynamics in cancer.

Highlights

- A comprehensive proteomics workflow was developed to study matrix stiffness in CRC.
- Matrix stiffness highly modulates secreted proteins with minimal effect on the intracellular proteome.
- Stiffness-induced secretome changes promote tumorigenic and metastatic properties.
- Mechanosensitive secretory phenotypes could represent novel targets in CRC.

2026, Mol Cell Proteomics *25*(*3*), 101515

https://doi.org/10.1016/j.mcpro.2026.101515

Deciphering Stiffness-Driven Changes in Colorectal Cancer by Proteomics

Charlotte Cresens[1,‡], Ana Montero-Calle[2,‡], Guillermo Solís-Fernández[1,2,‡], Behrad Shaghaghi[3], Lotte Gerrits[3,4], Samet Aytekin[1], Paul H. J. Kouwer[3], Rodrigo Barderas[2,5,*], and Susana Rocha[1,*]

Tumor stiffening plays a pivotal role in cancer progression. Increased tumor stiffness, resulting from interactions between cancer cells and their surrounding microenvironment, alters the tumor's mechanical properties and significantly impacts cancer growth and metastasis, the primary cause of cancer-related death. Despite the importance of tumor stiffness, systematic studies exploring its effect on protein dysregulation are limited. In this study, focused on colorectal cancer, we show by in-depth proteomics that matrix stiffness significantly alters the expression of secreted proteins, while intracellular protein levels remain largely unaffected. Functional assays reveal that the changes observed by proteomics in the secretome, driven by matrix stiffness, enhance cell migration, angiogenesis, and matrix remodeling, which collectively would contribute to a more aggressive cancer phenotype in a real scenario. Our findings emphasize the critical role of matrix stiffness in driving colorectal cancer progression through changes in the secretome, offering valuable insights for the development of biomechanical cancer therapies.

Colorectal cancer (CRC) ranks as the second most prevalent cancer in Europe when considering incidence rates across both genders (1–3). Predominantly sporadic, less than 5% of cases occur in individuals with a hereditary predisposition. Despite the reduction in mortality rates over the past decade, owing to screening programs and advancements in treatments for both adjuvant and metastatic disease, CRC remains the second leading cause of cancer-related deaths, surpassed only by lung cancer (4). Metastasis, the process by which cancer cells spread from the primary site to other parts of the body, significantly contributes to CRC mortality. About one-third of CRC patients are diagnosed at an advanced stage, typically when the tumor has become stiffer and metastasis has already occurred. Since most patients with metastatic CRC require second- and third-line treatments as the disease progresses, the 5-years survival rate remains less than 10%. This high mortality rate underscores the importance of understanding and combating CRC metastasis, making the development of new approaches to study CRC metastasis essential.

Previous research has shown that matrix stiffness, a mechanical property of the extracellular matrix (ECM), plays a significant role in cancer progression, including CRC metastasis (5). Depending on the cancer type and stage of tumor progression, cancerous tissue can be up to 20 times stiffer than its healthy counterpart (6). For example, healthy colorectal tissue has stiffness of ≈1 kPa, but as CRC progresses, stiffness typically increases. Early-stage tumors (T1 and T2) exhibit values ranging from 1 to 12 kPa, while more advanced stages (T3 and T4) and tumors with metastases show values between 3 and 68 kPa (7). This increase in stiffness is mainly driven by reciprocal interactions between cancer cells and other types of cells within the tumor microenvironment, particularly cancer-associated fibroblasts (CAFs). These interactions promote the secretion of ECM proteins and enhance the activity of ECM-modifying enzymes (*e.g.,* matrix remodelings (MMPs), disintegrin and metalloproteinase domain-containing proteins, tissue inhibitor of metalloproteinases (TIMPs), lysyl oxidase, and transglutaminases. Additionally, cellular traction forces further stiffen the tumor by aligning ECM fibers (8–11). The stiffened ECM has profound effects on cancer progression and metastasis, promoting the proliferation of tumor-initiating cells, epithelial-mesenchymal transition, alterations in extracellular vesicles, and various biochemical and biophysical changes in the tumor microenvironment (12–16).

Despite its recognized importance, no study has yet systematically explored the effect of substrate stiffness at protein level across the secretome, with previous work restricted to cell extracts or extracellular vesicles and outside the context of CRC (17–21). In this study, we examine by in-depth

From the [1]Molecular Imaging and Photonics Division, Chemistry Department, Faculty of Sciences, KU Leuven, Heverlee, Belgium; [2]Chronic Disease Programme, UFIEC, Instituto de Salud Carlos III, Madrid, Spain; [3]Molecular Materials Group, Institute for Molecules and Materials, Faculty of Science, Radboud University, AJ Nijmegen, The Netherlands; [4]Institute for Chemical Immunology, AJ Nijmegen, The Netherlands; [5]CIBER Frailty and Healthy Aging (CIBERFES), Madrid, Spain

‡Co-first, contributed equally.

*For correspondence: Rodrigo Barderas, r.barderasm@isciii.es; Susana Rocha, susana.rocha@kuleuven.be.

https://doi.org/10.1016/j.mcpro.2026.101515

proteomics analyses the effect of increased substrate stiffness on CRC progression using the KM12 cell model of CRC metastasis, and particularly the KM12L4a cell line, known for its high metastatic potential to liver and lung in nude mice, and its poorly metastatic isogenic counterpart, KM12C (22, 23). The KM12 model successfully replicates key aspects of CRC metastasis, and comprehensive analysis of its transcriptome and proteome have provided valuable insights into the metastatic process (24–32). To explore stiffness-induced changes, we grow these cells on synthetic polyacrylamide (PAAm) hydrogels with varying stiffnesses, representative of different stages of CRC development and progression. We analyze the intracellular and secreted protein content by mass-spectrometry based quantitative proteomics using the Orbitrap Exploris 480 mass spectrometer. Our study enabled a comprehensive in-depth analysis of changes in protein expression, functionality, and interactions related to stiffness. We extend our proteomic analysis using human cytokines antibody microarrays, validating our proteomics results through orthogonal techniques such as dot blot and ELISA. Finally, we perform functional cell-based assays to validate proteomic findings related to the dysregulation of tumorigenic and metastatic properties (angiogenesis, adhesion, ECM production and degradation, and cell migration) due to substrate stiffness. Therefore, this study underscores the significant role of ECM stiffness in CRC development and progression, highlighting that understanding these processes and targeting elements of the physical tumor microenvironment, including matrix stiffness, could be key to overcoming drug resistance and unlocking new avenues for therapeutic development (33).

EXPERIMENTAL PROCEDURES

Experimental Design and Statistical Rationale

All experiments were designed to ensure reproducibility and statistical robustness across biological and technical replicates. For the Tandem Mass Tags (TMT)-based quantitative proteomics analysis, three independent biological replicates (R1–R3) of KM12L4a cells were analyzed per stiffness condition (2, 21, 37, 47, and 56 kPa, and collagen-coated glass), yielding a total of 18 secretome and 18 cellular samples. Each biological replicate corresponded to an independent cell culture and hydrogel preparation, processed and analyzed separately.

Protein digestion, labeling, and LC-MS/MS acquisition were performed with the indicated biological replicates to minimize analytical variability. Statistical analyses were performed on normalized reporter ion intensities using moderated *t*-tests (false discovery rate [FDR], $\leq$0.05) to identify significantly dysregulated proteins with fold change $\geq$1.5 or $\leq$ 0.67. For dot blot, cytokine array, and ELISA validations, 6 biological replicates of KM12L4a cells (R1–R6) and 2 replicates of KM12C cells (R1–R2) were included, each analyzed with two technical replicates. Functional assays (wound healing, angiogenesis, and gelatin degradation) and qPCR analysis were performed with at least three biological replicates per condition, each including multiple fields of view or independent experimental wells. The selected number of replicates provided sufficient statistical power ($\geq$0.8) to detect differences of 1.5-fold or higher with $p \leq 0.05$, ensuring the reliability and reproducibility of the conclusions drawn from the proteomics and validation experiments.

Polyacrylamide (PAAm) Hydrogels

Hydrogel Synthesis—PAAm hydrogels were prepared as large, unattached gels as previously reported (34, 35). Briefly, acrylamide (Merck, A4058) and N,N′-methylenebisacrylamide (Merck, M1533) were dissolved in distilled water (dH_2O), sonicated on ice for 10 min and polymerized at room temperature using ammonium persulfate (Bio-Rad, #1610700EDU) and N,N,N′,N′-tetramethylethylenediamine (TEMED, Merck, T7024) in Petri dishes (92 x 16 mm, Sarstedt, 82.1473.001). The gels were stamped into either a 75 mm diameter for large-batch cell culture applications, or multiple 20 mm circular gels for rheological characterization. Stamped gels were washed with 10 ml dH_2O (3×), and incubated in 100 ml Dulbecco's Phosphate Buffered Saline (D-PBS, Thermo Fisher Scientific, 14200075) at 37 °C overnight to swell.

Hydrogel Characterization—PAAm hydrogels were characterized using a stress-controlled rotational rheometer (TA Instruments, Discovery HR-2), equipped with a 20 mm parallel plate geometry (DHR & AR-G2, Stainless Steel, 20 mm Plate, NST, 511,200.906) (34, 35). To prevent slippage, sanding paper hydrated with 1 ml D-PBS was attached to the plates. A swollen hydrogel, restamped into a 20 mm circles, was aligned on the rheometer and compressed 3%. A 30-s time sweep measurement was performed at 21°, 1% strain and 1 Hz frequency. Hydrogel stiffness (Youngs' modulus, E) was calculated from the storage modulus (G') using the formula: $E \approx 2\,G'\,(1+\nu)$,

TABLE 1
PAAm hydrogels

Name	Composition				Stiffness
	% AAm	% MBAA	% APS	% TEMED	Young's modulus (kPa)
2 kPa	5.00%	0.15%	0.25%	0.25%	2.2 ± 0.3
21 kPa	10.50%	0.45%	0.25%	0.25%	20.9 ± 2.9
37 kPa	18.00%	0.40%	0.25%	0.25%	36.7 ± 4.3
47 kPa	23.00%	0.45%	0.25%	0.25%	47.2 ± 5.5
56 kPa	28.90%	0.50%	0.25%	0.25%	56.1 ± 6.8

Gel compositions are given in final concentrations (AAm, MBAA, and APS in percentages; TEMED as V/V ratio). Average stiffnesses and errors were determined using a rotational rheometer with at least three technical replicates. Characterization details are in Supplemental Table S1.

AAm, acrylamide; APS, ammonium persulfate; MBAA, N,N′-methylenebisacrylamide.

where ν denotes the Poisson's ratio (approximately 0.5 for PAAm gels) (36, 37). Stiffness values and standard errors [average*(standard deviation/maximum)] were calculated from at least three technical replicates (Table 1, Table S1 for full dataset).

Hydrogel Functionalization—A swollen PAAm hydrogel was restamped into a 75 mm circular gel, placed in a Petri dish with 92 mm diameter, washed with 10 ml dH_2O (3×), and incubated under 365 nm UV-light for 15 min with 666 μg sulfosuccinimidyl 6-(4-azido-2-nitrophenylamino)hexanoate (sulfo-SANPAH, Merck, 803,332) diluted in 10 ml sterile dH_2O, (to a 0.1 mg/cm^2 coating density). This step was repeated with a fresh sulfo-SANPAH solution, resulting in a rust-brown gel. After washing with 10 ml sterile dH_2O (3×), the gel was incubated overnight with 165 μg collagen type I (Thermo Fisher Scientific, A1048301) diluted in 10 ml sterile 0.5% acetic acid (Acros Organics, 64–19–7, 99.8%, pH 3.40) to ensure homogeneous coating (25 μg/cm^2 coating density) (38). The coated gel was then washed with 10 ml sterile D-PBS (3×) and equilibrated in 10 ml prewarmed sterile cell culture medium at 37 °C and 5% CO_2 for at least 30 min before cell seeding. Collagen-coated glass controls were prepared in a glass-bottom 6-well plate with wells of 35 mm diameter (Cellvis, P06–1.5H-N), by washing with dH_2O (3×), incubating overnight with 23.9 μg collagen type I per well (Thermo Fisher Scientific, A1048301) diluted in 1.45 ml sterile 0.5% acetic acid (Acros Organics, 64–19–7, 99.8%, pH 3.4) to ensure the same coating density as on the PAAm gels. After overnight incubation, the plate was washed with dH_2O (3×) and equilibrated in cell culture medium, as was done for the PAAm gels.

Cell Culture

Cell Lines—Isogenic KM12C and KM12L4a colorectal cancer cell lines (Fidler's lab, MD Anderson Cancer Center), immortalized human primary colorectal cancer-associated fibroblasts (CAFs, more specifically CT5.3, De Wever's lab), and green fluorescent Human Umbilical Vein Endothelial Cells (TTFLUOR HUVEC, Innoprot) were used (22, 23, 39). All cell lines, except HUVEC, were cultured in Dulbecco's Modified Eagle Medium (DMEM, Thermo Fisher Scientific, 31,053,028) with 10% fetal bovine serum (FBS, Merck, F7524), 1% GlutaMAX (Thermo Fisher Scientific, 35,050,038), and 0.1% Gentamycin (Carl Roth, 2475.1). HUVECs were grown in endothelial cell basal medium (EBM-2, Lonza, CC-3156) with 2% FBS, hydrocortisone, human fibroblast growth factor-B, vascular endothelial growth factor (VEGF), long arginine 3-insulin-like growth factor-1, ascorbic acid, human epidermal growth factor, gentamicin sulfate-amphotericin, and heparin (complete EBM-2 medium) according to the manufacturers' instructions (EGM-2 SingleQuots Supplements, Lonza, CC-4176). All cells were maintained in a humidified incubator at 37 °C and 5% CO_2. HUVECs were used up to passage 2.

Seeding, Growing, and Starving Cells on PAAm Gels—10 million KM12C or KM12L4a cells were seeded on a 75 mm equilibrated PAAm gel at approximately 1.5 x 10^6 cells/cm^2 and cultured for 24 h in a humidified incubator at 37 °C and 5% CO_2. For starvation, cells were washed twice with 10 ml prewarmed D-PBS (1×) and transferred to a new Petri dish to remove runoff cells. The gel was washed again and incubated in 13 ml prewarmed serum-free medium for 48 h to eliminate serum interference. Cell viability was assessed after 48 h of serum-free incubation across all conditions using trypan blue. Viability remained above 80% in all cases, and no detectable morphological changes or losses of adherence were observed.

Secretome and Cell Collection—To analyze exclusively the secreted proteins from viable adherent cells, all detached, floating, and dead cells were removed from the starved medium by centrifugation (5 min, 140 g). The resulting supernatant was subsequently frozen at −80 °C following an identical protocol for all conditions. A 10 ml portion was concentrated 10× via freeze-drying and resuspended in 1 ml sterile MilliQ water for analysis. Cells were washed with 10 ml prewarmed D-PBS (3×) and their morphology monitored by taking brightfield images on a Leica DM IL LED (https://www.leica-microsystems.com/products/light-microscopes/p/leica-dm-il-led/) microscope using a 10× air lens (Leica HI PLAN, NA 0.22). Cell segmentation was performed using iLastik and manually training a model to identify the regions corresponding to cell aggregates. For the iLastik analysis, three training sets were made, one for the control, one for the stiffer substrates, and a third one for the softer substrates. Each model was then used to analyze the corresponding images. Next, the masks obtained with this segmentation model were analyzed with an in-house written python script to obtain their area, perimeter, and circularity. Finally, the data on these variables was plotted and tested for statistical significance using GraphPad Prism (Kruskal-Wallis test comparing the mean differences of all samples to the control condition). For cell collection, cells were detached by repeatedly flowing 10 ml prewarmed 4 mM EDTA (Thermo Fisher Scientific, J15694.AE) over the gel, and detachment was confirmed via brightfield microscopy. The gel was rinsed with 3 ml D-PBS, and this solution was combined with the cell suspension collected before. Cells were pelleted (5 min, 140 g) and resuspended in 500 μl D-PBS. A 10 μl aliquot was taken for cell counting and viability assessment using trypan Blue. The remaining suspension was centrifuged again to collect a dry pellet, which was subsequently frozen at −80 °C.

Immunofluorescence

Protein expression and subcellular localization in cells grown on PAAm gels were visualized using immunolabelling (35, 40). Gels were fixed in 4% paraformaldehyde (Thermo Fisher Scientific, 28,908), permeabilized with 0.1% Triton X-100 (Merck, T8787), and blocked with a blocking buffer (Table S2. Primary and secondary antibodies (Table S2 were used, followed by 4′,6-Diamidino-2-Phenylindole (DAPI, Thermo Fisher Scientific, D1306) staining. Samples were mounted in a glass-bottom 6-well plate (Cellvis, P06–1.5H-N) with ~1.2 ml D-PBS for imaging.

Imaging was performed on a Leica TCS SP8 microscope with a 63 × water immersion objective (NA: 1.2). Excitation occurred at 405 nm (DAPI) and 638 nm (Abberior STAR RED), and emissions were captured using hybrid detectors. Z-stacks were acquired with 512 × 512 pixels, 200 Hz line scan speed, and 4-line averaging. Tubulin signal was quantified using Imaris Viewer software (Oxford Instruments, https://imaris.oxinst.com/imaris-viewer), with segmentation and analysis of DAPI and tubulin fluorescence, 3D volume, and sphericity. Collagen signal was quantified using a trainable Weka segmentation in Fiji (ImageJ, https://imagej.net/software/fiji/downloads) and measuring the mean signal intensity on the regions of interest. Detailed procedures are provided in the Supporting Information.

Protein Extraction and Quantification

Proteins were extracted from the collected pellets using radioimmunoprecipitation assay buffer (RIPA buffer, Sigma-Aldrich, R0278), with 1:100 v/v of proteases and phosphatases inhibitor cocktails (MCE, HY-K0022 and HY-K0010), followed by centrifugation (10 min at 10,000 g, 4 °C) to remove cell debris. Protein extracts were quantified using the Tryptophan fluorescence method, and quality and concentration were confirmed by loading 5 μg of protein extract on a 10% SDS-PAGE gel under reducing conditions, with the PageRuler Plus Prestained Protein Ladder (Thermo Fisher Scientific, 26,619) and Coomassie blue staining (41).

TMT Labeling

Cell extracts (10 μg in 100 μl RIPA) and secretome samples (900 μl) from FBS-free DMEM were used for TMT labeling. Proteins were reduced with 10 mM tris-(2-carboxyethyl)phosphine, hydrochloride (45 min, 37 °C, 600 rpm) and alkylated with 40 mM chloroacetamide

(30 min, room temperature, 600 rpm, protected from light). Three replicates per condition (R1-3) were processed.

Proteins were bound to magnetic beads (50% hydrophilic, 50% hydrophobic) in acetonitrile, washed, and digested overnight at 37 °C with porcine trypsin (Thermo Fisher Scientific). After digestion, samples were labelled with 18 (TMT) in two incubation steps (30 min, room temperature), quenched with glycine, and fractionated. Peptides were reconstituted in 0.1% FA and injected into the LC-MS/MS system. Further experimental details are provided in the Supporting Information.

LC-MS/MS Analysis

LC-MS/MS analysis was performed using an Orbitrap Exploris 480 mass spectrometer coupled with a Vanquish Neo UHPLC System for peptide separation (Thermo Fisher Scientific). Peptides were analyzed with a 2-h gradient using 0.1% FA in MilliQ water and 0.1% FA in 80% aceronitrile as buffers. Mass spectra were searched against the Uniprot *Homo sapiens* database using MaxQuant (v2.4.2), with trypsin as the digestion enzyme, stringent FDR thresholds of 0.01 for peptide identification, and a fragment ion mass tolerance of 20 ppm for MS/MS spectra. Protein quantification was performed with reporter ion intensities bias-corrected for TMT reagents. For TMT-based quantification, reporter ion intensities were extracted using a reporter ion mass tolerance of 0.03 Da. Statistical analysis included Bayes-moderated t-tests and filtering for proteins identified in $\geq$60% of samples, with significant dysregulated proteins defined by expression ratio cutoffs of $\geq$1.5 or $\leq$0.67 and FDR $\leq$0.05. Single-peptide identifications were retained in the analysis when the peptide was of sufficient length ($\geq$7 amino acids), had a high confidence score (FDR <1%), and no ambiguous matches (see Fig. S1 for annotated spectra obtained with the Proteomics Data Viewer software (PDV-2.2.0 software, github.com/wenbostar/PDV).

Dysregulated proteins were analyzed with STRING and Reactome, whereas SecretomeP 2.0, SignalP 6.0, and the ExoCarta database were used for the analysis of secretion pathways (42–51). STRING provided network-based predictions of protein-protein interactions, integrating both experimental evidence and computational inference. Reactome offered high confidence, manually curated pathway annotations. Gene Ontology (GO) enrichment analyses facilitated broad biological categorization. Likewise, SecretomeP 2.0, and SignalP 6.0 enabled the prediction of nonclassical and classical secretion routes, respectively. Finally, ExoCarta provided experimental evidence of exosome-associated proteins from published datasets. To overcome the constraints of relying on prediction-based or single-source experimental tools, we employed multiple complementary platforms, allowing us to cross-validate results and reinforce the reliability of the functional interpretation. Further details on the LC-MS/MS setup, data processing, statistical analysis, and pathway annotations are available in the Supporting Information.

Data dependent acquisition files and MaxQuant searches of the two TMT quantitative proteomics analysis have been deposited to the ProteomeXchange Consortium via the PRIDE partner repository with the dataset identifier PXD064023 (52).

Dot Blot

For validation of the dysregulation of selected proteins, we performed a dot blot with the 6 replicates of KM12L4a cells (KM12L4a R1-6) and the 2 replicates of KM12C cells (KM12C R1-2). For dot blot, 5 µl or 25 µl nonlyophilized secretome diluted in D-PBS to a total volume of 100 µl, was blotted onto a nitrocellulose membrane using the Bio-Dot 96-Well Microfiltration Apparatus (Bio-Rad, 72,926–1). Protein transfer was verified by Red Ponceau staining (Merck, P3504). Membranes were blocked in blocking buffer (Table S2 on a seesaw rocker plate for 1 h at room temperature, and incubated with primary antibody diluted in blocking buffer (Table S2 on a seesaw rocker plate overnight at 4 °C. Then, membranes were washed three times with 0.1% Tween 20 diluted in D-PBS for 10 min each, and incubated with the appropriate HRP-conjugated secondary antibody (Table S2 diluted in blocking buffer on a seesaw rocker plate for 1 h at room temperature. Membranes were washed three times with 0.1% Tween 20 diluted in D-PBS for 10 min each, and the signal was developed using the ECL Pico PLUS Chemiluminescent Substrate (Thermo Fisher Scientific, 34,580) or, alternatively, the SuperSignal West Femto Maximum Sensitivity Substrate (Thermo Fisher Scientific, 34,096). Images were recorded on an Amersham ImageQuant 800 (Cytiva). For image quantification, the integrated density inside an equally sized circular region was measured for the different dots in Fiji (ImageJ), simultaneously analyzing 2 and 47 kPa dots from the same replicate (53). For each replicate, the image with optimal exposure conditions was analyzed and data was plotted as the ratio of 47 versus 2 kPa.

Cytokine Array

Secretome from 2 and 47 kPa nonlyophilized samples were directly analyzed using the Human Cytokine Antibody Array C5 kit (RayBiotech, AAH-CYT-5-8), according to the manufacturers' instructions. Three replicates were analyzed per condition (KM12L4a R1-3). Briefly, 0.9 ml secretome were incubated overnight at 4 °C on an antibody microarray previously blocked with the supplied blocking buffer. After the washing steps, the biotinylated antibody cocktail was incubated overnight at 4 °C. After new washing steps, HRP-streptavidin was incubated for 2 h at room temperature. After final washing steps, the chemiluminescence detection was developed and recorded immediately afterward on an Amersham ImageQuant 800 (Cytiva). Signal quantification was performed with the gel analysis tool in Fiji (ImageJ), simultaneously analyzing corresponding rows of aligned 2 and 47 kPa membranes from the same replicate (53, 54). For each spot, the image with optimal exposure conditions was analyzed and data was plotted as the ratio of 47 versus 2 kPa.

ELISA

For validation of the results obtained by antibody microarrays, secretome from 2 and 47 kPa nonlyophilized samples were surveyed by ELISA, according to the manufacturer's instructions, to determine the protein levels of VEGF, IL-8, CXCL1, and osteoprotegerin (OPG) in 6 replicates of KM12L4a cells (KM12L4a R1-6) and 2 replicates of KM12C cells (KM12C R1-2). Human IL-8 sandwich ELISA kit (Proteintech, KE00006) and human CXCL1 sandwich ELISA kit (Proteintech, KE00133) were used with 25 µl secretome samples diluted 1:2 in PT 4-eg sample diluent and PT 1-ef sample diluent (provided in the kit), respectively. Additionally, 5 µl and 10 µl secretome samples 1/10 and 1/5 diluted in sample diluent (provided in the kit) were analyzed using the human VEGF sandwich ELISA kit (Proteintech, KE00216) and the human OPG ELISA kit (Elabscience, E-EL-H1341), respectively. Color was developed according to the manufacturer instructions and signal recorded onto a Spark multimode microplate reader (Tecan Trading AG).

RNA Extraction, cDNA, and qPCR Analyses

For RNA extraction, CRC cells were pelleted as indicated above. Then, cell pellets were re-suspended in 500 µl of NZYol reagent by pipetting up and down, and incubated 5 min at RT. Subsequently, 100 µl of chloroform (Sigma-Aldrich) was added per sample, mixed by inversion, and incubated 3 min at RT. After centrifugation at 12,000*g* and 4 °C for 15 min, the upper phase, containing the isolated RNA, was transferred to a new tube, mixed with 1× volume of 70% ethanol, and purified using the RNeasy Mini Kit (Qiagen) following

manufacturer's instructions. RNA concentration was quantified in Nanodrop One (Thermo Fisher Scientific), and samples stored at −80 °C until used.

cDNA synthesis was performed from 500 ng of total RNA using the NZY First-Strand cDNA Synthesis Kit (NZYtech) following manufacturer's instructions. For qPCR analyses, 2 µl of 1:5 diluted cDNA was used for quantification of mRNA levels of targeted genes (Supplemental Table S3), using 5 µl of TB Green Premix Ex Taq II (Takara) and 0.2 µl of each 10 µM oligonucleotide per reaction, as previously optimized (55). Light Cycler 480 (Roche) was used for qPCR analyses, using the 18S gene as control and for normalization. Three biological replicates of each condition (glass, 2 kPa, and 47 kPa with and without 48 h starvation) were analyzed in duplicate (technical replicates) in the qPCR analysis.

Functional Assays

Wound Healing—KM12C cells were seeded into wound healing inserts (Ibidi, #80209) in a plastic-bottom 24-well plate (Sarstedt, 83.3922) at a density of 1.5 x 10^5 cells per insert (3 x 10^5 per well). The next day, the inserts were removed to uncover a cell-free area of 500 ± 100 µm. 500 µl of fresh cell growth medium was added, along with 5 µl of lyophilized secretomes (KM12L4a R1 and R4) or control (lyophilized starvation medium). Time-lapse imaging was performed using a Leica THUNDER imager with a 10× air objective (NA: 0.32) at 37 °C and 5% CO_2. Images (1024 x 1024 pixels, 1327 x 1327 µm) were acquired every hour and analyzed using the MRI's Wound Healing tool for Image J software (NIH) (https://github.com/MontpellierRessourcesImagerie/imagej_macros_and_scripts/wiki/Wound-Healing-Tool). Cell-free areas were visually inspected, and wound closure speed was calculated from the slope of the linear segment of the area vs. time plot.

Angiogenesis—A 15-wells µ-Slide angiogenesis chamber (Ibidi, 81,506) was coated with 10 µl Matrigel (Merck, CLS356234) and incubated for 1 h at 37 °C and 5% CO_2. TTFLUOR HUVECs were harvested with trypsin and centrifuged (5 min at 140 g), and 2 x 10^4 cells were resuspended in 25 µl complete EBM-2 medium. Per condition, 25 µl of lyophilized secretome (1.5 µl secretome in 23.5 µl D-PBS) was added. The positive control contained only complete EBM-2 medium. The mixture was added onto the Matrigel-coated coverslip. Of note, dilution of the secretomes also diluted angiogenic factors in the EBM-2 medium, potentially affecting tube formation. The secretome of both KM12L4a and KM12C CRC cells cultured on 2 kPa (soft) and 47 kPa (stiff) substrates was used. Each condition was analyzed in duplicate.

Tube formation was monitored via time-lapse imaging on a Leica THUNDER imager with a 10 × air objective (NA: 0.32) under incubation at 37 °C and 5% CO_2. GFP-channel images (1024 × 1024 pixels, ~1325 × 1325 µm) were acquired every 5 min over 6 h across 9 fields of view per condition. Images were analyzed in Fiji by enhancing contrast, subtracting the background, applying a 3-pixel radius median filter, automatic thresholding, two iterations of erosion, and watershed segmentation (53). The area of individual features was quantified and normalized to the mean area at timepoint 0. Incremental changes of the normalized area over time were determined via a linear fit in Microsoft Excel, and normalized to the median of the control condition.

Gelatin Degradation—Coverslips coated with fluorescently labeled gelatin were prepared based on a protocol kindly provided by Prof. E. Planus (56, 57). Briefly, 12 mm round glass coverslips (VWR, 631–1577) were cleaned, sterilized under UV-light, and coated with 25 µg poly L-lysine (Merck, P8920) for 20 min at room temperature. After washing, coverslips were fixed with 0.5% glutaraldehyde (Alfa Aesar, A17876) for 15 min on ice, washed, and coated with a mixture of nonfluorescent gelatin (Merck, G1890) and FITC-conjugated gelatin (AnaSpec, AS-85145), each at 0.2 mg/ml. Coverslips were incubated with this mixture for 10 min, washed with D-PBS, and sterilized under UV light for 5 min.

CAF CT5.3 cells, labeled with cell tracker red CMTPX (Thermo Fisher Scientific, C34552), were seeded at 1 × 10^4 cells per coverslip in 500 µl medium containing 5 µl lyophilized secretome (KM12L4a R1 and R4–6) or control (lyophilized starvation medium). Alternatively, KM12L4a cells were directly used in the assay in 500 µl standard medium alone to assess their intrinsic degradation activity. After 48 h incubation at 37 °C and 5% CO_2, gelatin degradation was imaged using a Leica TCS SP8 microscope with a 20 × air objective. Z-stacks (512 × 512 pixels) were acquired sequentially in the FITC (488 nm excitation) and cell tracker red (552 nm excitation) channels.

Further experimental details, including image analysis and quantification methods, are provided in the Supporting Information.

Statistical Analyses

Statistical analyses were performed in GraphPad Prism 10 (GraphPad, www.graphpad.com/), except when stated otherwise. For dot blots, cytokine arrays, qPCRs, ELISAs, and intracellular collagen, a one-sided *t* test with unequal variances and a hypothetical mean of 1 (Welch's *t* test) was performed in Microsoft Excel and used to evaluate whether the observed ratios (*e.g.,* 47 kPa vs 2 kPa) significantly deviated from 1, representing no change. Unequal variance was assumed due to the inherent variability of biological replicates. This choice was based on *a priori* directional hypotheses derived from the proteomic analysis (*i.e.,* expected up- or downregulation), making the validation assays confirmatory rather than exploratory. The one-sided test thus provided appropriate sensitivity while maintaining control of Type I error for directionally constrained comparisons (58). For 3D cell morphology and cytoskeleton analyses, unpaired nonparametric t-tests were applied to compare independent experimental conditions. Data normality was tested using the Shapiro–Wilk test, and accordingly, either a parametric test with Welch's correction or a nonparametric Mann–Whitney test was used. For wound healing and angiogenesis assays, one-way ANOVA was employed to assess significant differences across three or more groups under a single factor (substrate stiffness). For gelatin degradation assays, a nonparametric Kruskal–Wallis test was used to compare mean ranks across groups, followed by an uncorrected Dunn's post-hoc test, as data did not meet the assumptions of normality and homoscedasticity required for ANOVA. Plots were made in GraphPad Prism or according to the SuperPlots tool that displays the data distribution according to its replicates and visually represents its reproducibility (59). All significances were evaluated as follows: nonsignificant difference for $p > 0.05$ (–), significant difference for $p \leq 0.05$ (*), significant difference for $p \leq 0.01$ (**), significant difference for $p \leq 0.001$ (***), significant difference for $p \leq 0.0001$ (****).

RESULTS

Replicating CRC Stiffnesses with PAAm Hydrogels

To mimic the changes in ECM stiffness observed in CRC progression, we developed a library of synthetic PAAm hydrogels. These hydrogels, produced as large, free-standing gels, are easily customizable in both shape and size, rendering them ideally suited for different applications, namely proteomic analysis and multiplexed immunolabeling (34, 35). The stiffness of the synthesized PAAm gels was tuned by varying the acrylamide and N,N′-methylenebisacrylamide content, and measured using a rotational rheometer (Table 1, and Experimental Procedures and

Supplemental Table S2 for details). The softest gel (2 kPa) mimics the stiffness of healthy colorectal tissue, whereas the stiffer gels (21–56 kPa) simulate the stiffness of advanced CRC (stages T3 and T4) (7).

Culturing metastatic KM12L4a CRC cells on collagen functionalized PAAm gels and collagen-coated glass (control) revealed substantial differences in cell morphology depending on the substrate stiffness. Cell aggregates formed under

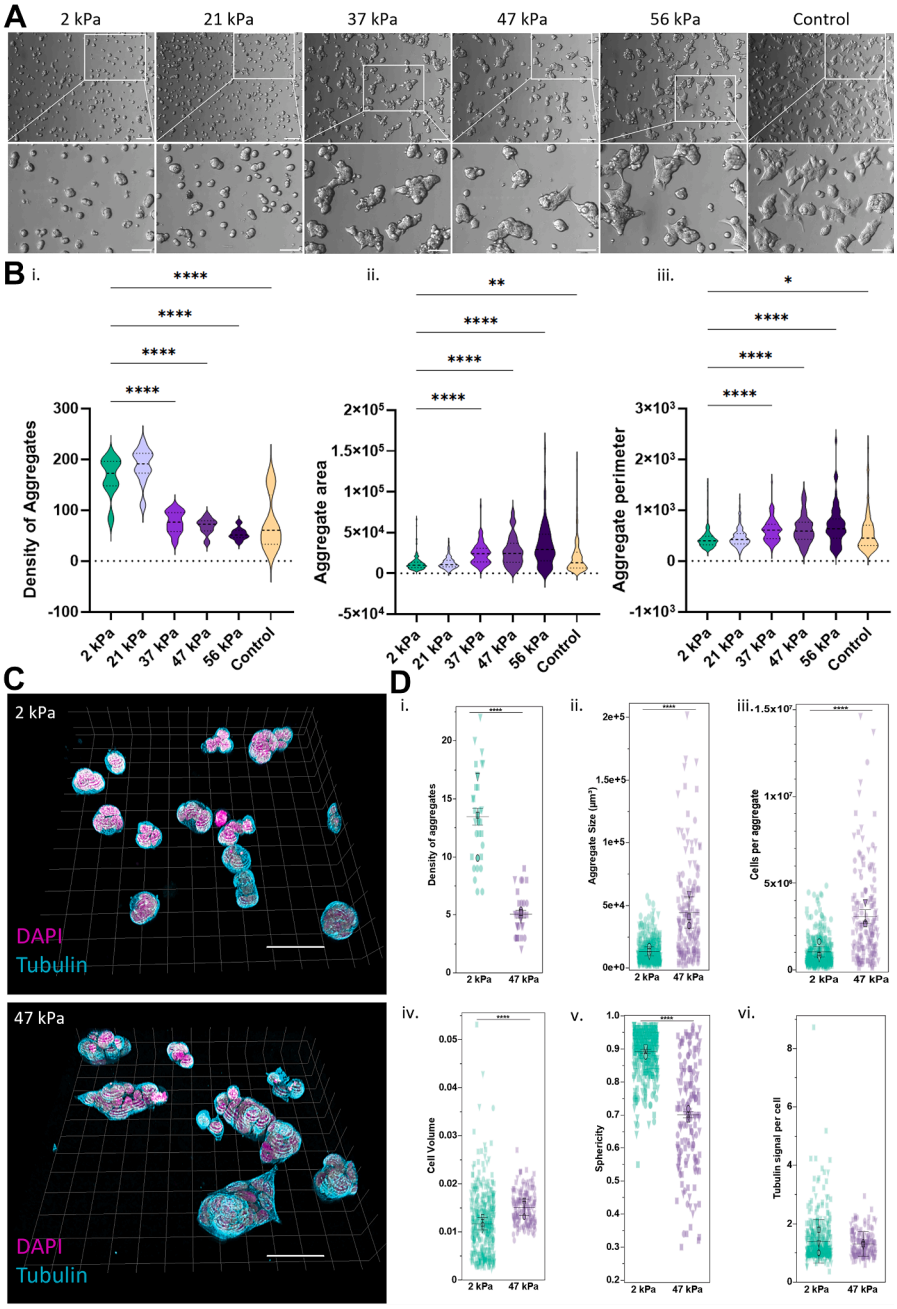

FIG. 1. **Growth of metastatic KM12L4a cells on top of collagen functionalized PAAm hydrogels, and collagen-coated glass (control).** Images are representative of cells before proteomic analysis: after 24 h cell growth, 48 h starvation, and three washes with D-PBS. *A*, representative transmission images. These scale bars represents 200 µm and 100 µm, for full size and magnifications, respectively. *B*, brightfield quantification of cell aggregate morphology (density, area, perimeter). Data is represented in a *violin* plot where *solid lines* show medians, while *dashed lines* show quartiles. Data was obtained from minimally 2 fields of view, from three biological replicates. *C*, representative 3D view of tubulin (*cyan*) and 6-Diamidino-2-Phenylindole (*magenta*) in KM12L4a cells grown on 2 and 47 kPa hydrogels. Grid represents 3D-view, with XY scale bar represents: 50 µm. *D*, 3D morphological quantification for different parameters. Data was obtained from n = 30 samples, from three biological replicates. *B* and *D*, significance levels: (–) $p > 0.05$, non-significant; (****) $p \leq 0.0001$.

all conditions, but quantitative analysis revealed that significantly more aggregates were present on softer substrates, and these aggregates were significantly smaller in terms of their area and perimeter (Fig. 1, *A* and *B* and Supplemental Fig. S2*A*). To investigate these differences in more detail, we focused on two stiffness values (2 and 47 kPa) with clear differences in aggregate formation. To assess if cytoskeletal changes were driving the observed morphological differences, we visualized 3D cell structure through labeling of tubulin or actin, major components of the cytoskeleton (Fig. 1, *C* and *D*, for tubulin, and Supplemental Fig. S2*B* for actin). Consistent with our initial observations, we found more and smaller aggregates on the softer substrates (Fig. 1*D*i-iii), with cells forming tightly packed, spherical aggregates (Fig. 1*D*iv-v). On stiffer substrates, particularly at the aggregate edges, cells spread out and exhibited cytoskeletal protrusions, even though the tubulin expression level remains similar to that on the softer substrate (Fig. 1*D*vi). Similar results and trends were observed for actin (Supplemental Fig. S2*B*). These results indicate that substrate stiffness influences cell morphology, underscoring that KM12L4a cells are mechanosensitive and therefore suitable for studying the impact of altered ECM stiffness.

Exploring Stiffness-Induced Changes on Protein Expression

In-Depth Quantitative TMT-Based LC-MS/MS Analysis—To investigate how substrate stiffness affects protein expression, we analyzed both cellular and secreted proteins by LC-MS/MS. KM12L4a cells were cultured for 72 h on collagen functionalized PAAm gels and on collagen-coated glass (control). During the final 48 h, the standard cell culture medium was replaced by serum-free medium to avoid FBS interference in the proteomic analysis. The experiments, performed in triplicate (R1-3), included PAAm hydrogels with five different stiffnesses and the glass control, resulting in 18 secretome and 18 cell samples. Cells were lysed with RIPA buffer and proteins were extracted. The quality of the cell protein extracts was verified by Coomassie blue staining prior to TMT-labeling (Supplemental Fig. S3). Secretome samples were processed separately by gentle centrifugation to remove detached and dead cells, ensuring high-quality samples for proteomics analysis.

After cell lysis, each cell protein extract and its paired secretome sample were separately reduced, alkylated, digested using trypsin, and labeled with one out of the 18 different TMT reagents. Then, the 18 TMT labeled samples were pooled together, and analyzed by LC-MS/MS on an Orbitrap Exploris 480 mass spectrometer. After normalizing the data (Supplemental Fig. S4), a total of 48,418 peptides were identified and quantified in the cell extracts (resulting in 6484 proteins), and 18,352 peptides in the secretome samples (resulting in 3333 proteins identified and quantified), in both cases with at least one unique peptide and an ion score above 99% (Supplemental Tables S4 and S5). Principal component analysis was then performed to investigate the variability among biological replicates and to compare the protein expression profile of cells cultured on the different stiffnesses. No clear separation was observed between the cell protein extracts of samples grown on different substrates (Supplemental Fig. S5*A*). In contrast, the TMT proteomic analysis of the secretome showed a clear separation with increasing substrate stiffness (Fig. 2*A*). The secreted protein profiles for 2 kPa and glass conditions were well-separated from each other and from the other stiffnesses. Notably, the principal component analysis positioned the 21 kPa condition together with the higher-stiffness hydrogels (37–56 kPa) and clearly separated from the 2 kPa condition. Given that 21 kPa lies within the pathophysiological range of advanced CRC tumors, we grouped all conditions $\geq$21 kPa into a single 'stiff' category for downstream analysis.

In parallel, we evaluated whether the 48 h serum-free period induced stress- or autophagy-related effects. Cell viability remained above 80% across all stiffness conditions and microscopy showed no detachment or autophagy-related morphological changes. qPCR analysis showed that starvation modulated several autophagy-related genes on glass and 2 kPa, while most of these genes remained unaltered on the 47 kPa stiffness gel (Supplemental Fig. S6). Notably, starvation triggered opposite transcriptional responses on glass versus 2 kPa, suggesting a stiffness-dependent adaptation to nutrient deprivation (Supplemental Fig. S6*A*). In addition, transcriptional profiles on 2 or 47 kPa gels relative to glass were similar with and without starvation (8 genes displayed a similar dysregulation trend at 2 kPa regardless of starvation, and 13 genes exhibited consistent dysregulation at 47 kPa). Only ANXA1 showed opposite regulation, possibly reflecting its involvement in biological processes beyond autophagy and secretion. Together, these results indicate that although autophagy is modulated by stiffness, it does not account for the stiffness-dependent changes in protein secretion.

Dysregulation Analysis Reveals Differences Between Soft and Stiff Substrates—For further analysis, proteins were considered as dysregulated in cell extracts or secretomes if their expression ratio was $\geq$1.5 (upregulated) or $\leq$ 0.67 (downregulated), and FDR was $\leq$0.05. A significant dysregulation was observed in the secretome of KM12L4a cells cultured on different stiffnesses compared to glass (Fig. 2*B*, Supplemental Fig. S7*A*, and Supplemental Table S4), whereas cell extracts showed almost no dysregulation (Supplemental Fig. S5, *B* and *D* and Supplemental Table S5). Interestingly, despite the low number of dysregulated proteins in cell extracts, both the cell extracts and the secretome showed that a higher number of proteins were dysregulated on the softer hydrogel compared to glass, *i.e.,* the stiffest condition. These results suggest that culturing cells on substrates with different stiffnesses, mimicking CRC

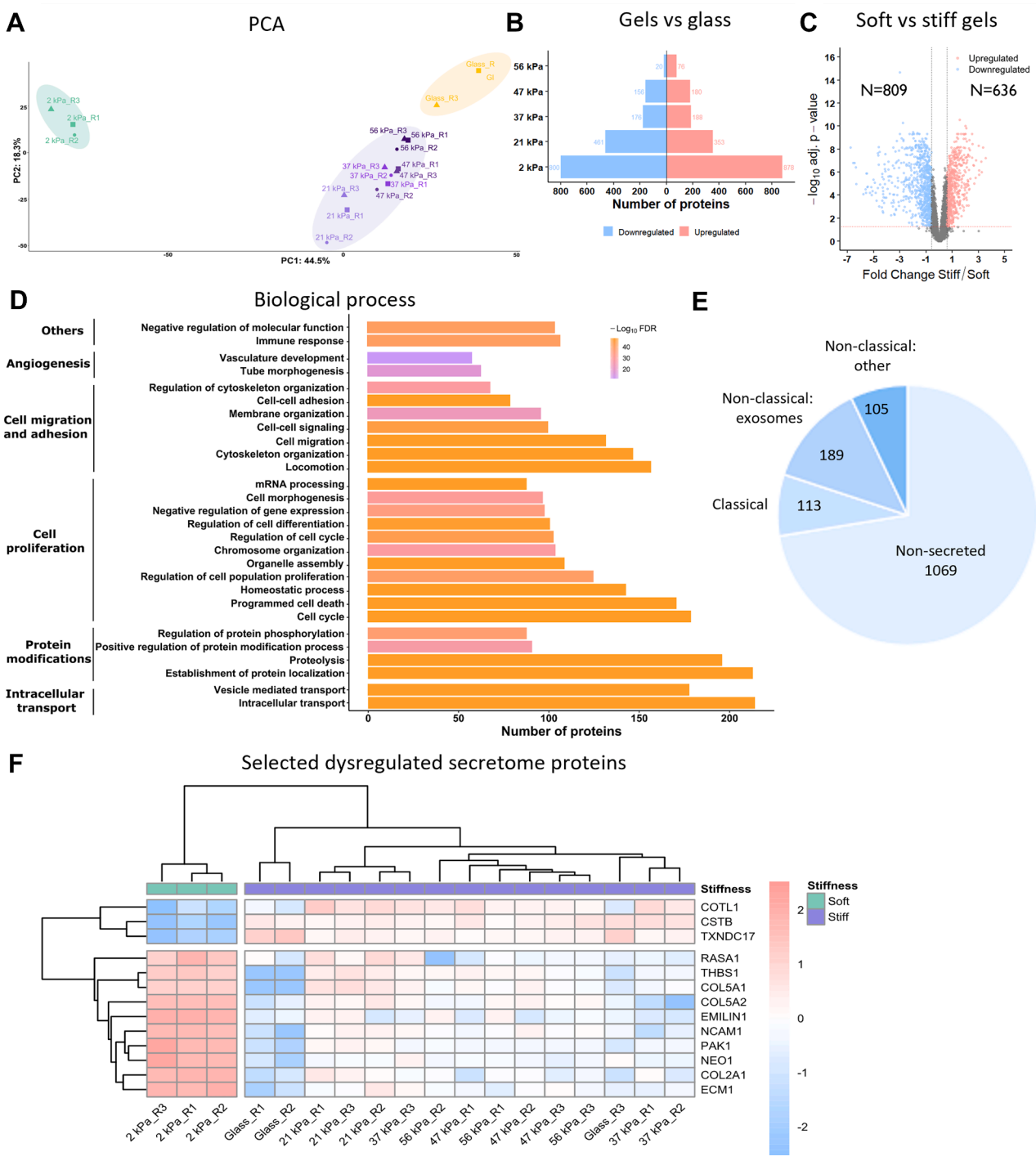

FIG. 2. **Proteomic analyses of secretome samples.** *A* and *C*, differential expression analyses. *A*, principal component analyses (PCAs) representing sample clustering according to the stiffness. *B*, bar plots with the number of upregulated (*red*) and downregulated (*blue*) proteins in the different stiffness conditions, compared to glass. Volcano plots with the fold changes and *p*-values are shown in Supplemental Fig. S5*A*. *C*, volcano plots of proteins identified and quantified as altered in stiff (21, 37, 47, and 56 kPa) *versus* soft (2 kPa) conditions. The x-axis represents the Log_2 expression ratio (fold change) of stiff *versus* soft relative protein expression ratios, the y-axis depicts the FDR value (adj. *p*-value) based on Log_{10}. Colored dots -represent differentially expressed proteins upregulated (*red*) and downregulated (*blue*) in stiff conditions with FDR $\leq$0.05 (represented by *red dashed horizontal line*) and 1.5-fold expression ratio (represented by *two black dashed vertical lines*). *D* and *F*, bioinformatics analysis of dysregulated proteins in stiff (21, 37, 47, and 56 kPa) versus soft (2 kPa) conditions. *D*, *bar plots* represents the most significantly enriched biological processes in which dysregulated proteins are involved according to Gene Ontology analysis. Cellular components and Reactome analysis are shown in Supplemental Fig. S5, *B* and *C*. *E*, location and secretion pathway analysis of dysregulated secretome proteins according to SecretomeP, SignalP, and ExoCarta databases. *F*, heatmap of the Tandem Mass Tags relative protein

development and progression, causes the cells to release different factors.

We proceeded by comparing the 2 kPa condition (mimicking healthy colorectal tissue, soft condition) to the four PAAm hydrogels with higher stiffnesses (21–56 kPa, advanced CRC stages T3 and T4, stiff conditions). Cell extracts showed minimal dysregulation, with only 3 upregulated and 3 downregulated proteins (Supplemental Fig. S5*C*). In contrast, the secretome exhibited extensive dysregulation between soft and stiff conditions, with 636 upregulated and 809 downregulated proteins (Fig. 2*C*). Therefore, our subsequent analysis was primarily focused on the dysregulated proteins within the secretome.

Then, we performed GO enrichment to identify the cellular components and biological processes where the 1445 dysregulated secretome proteins were involved (Fig. 2*D* and Supplemental Fig. S7*B*). Cellular component analysis revealed that the dysregulated proteins were present in various cellular locations, with a substantial number associated with vesicles (167 proteins), and the extracellular matrix and cell attachment (321 proteins) (Supplemental Fig. S7*B*). Moreover, intracellular transport mechanisms (247 proteins), protein alterations (370 proteins), cell proliferation (472 proteins), cell migration and adhesion (317 proteins), and angiogenesis (63 proteins) were the processes more highly enriched (Fig. 2*D*).

Notably, a large fraction of the dysregulated secretome proteins lacked classical signal peptides, and vesicle-related GO terms were enriched, suggesting potential involvement of autophagy or nonclassical secretion. Analysis of representative autophagy-related genes and proteins across stiffness conditions showed no significant changes relative to glass controls (Supplemental Fig. S6*B*), in agreement with the absence of autophagy pathway activation in the cellular proteome. We next examined representative markers of nonclassical secretion (ANXA1, BAG3, HMGB1, LGALS3, and SNAP23). ANXA1 and BAG3 were reduced on both soft (2 kPa) and stiff (47 kPa) substrates relative to glass, LGALS3 decreased only on soft matrices, while HMGB1 and SNAP23 were downregulated at 2 kPa but upregulated at 47 kPa. Although modest, these changes suggest stiffness-associated modulation of nonclassical secretory pathways. Together with preserved cell viability (>80%) and the absence of morphological signs of autophagic stress, these results support that the secretome dysregulation observed is primarily driven by stiffness-dependent modulation of secretory pathways, rather than by a generalized activation of autophagy.

The analysis of the dysregulated proteins using the Reactome database identified significant alterations in pathways involved in neutrophil degranulation (83 proteins), N-linked glycosylation (57 proteins), translation (56 proteins), mRNA splicing and rRNA processing (45 and 44 proteins, respectively), signaling by ROBO receptors (45 proteins), and programmed cell death (43 proteins) (Supplemental Fig. S7*C*).

Validating and Extending Secretome Dysregulation Analysis

Given the substantial changes observed in the secretome in response to substrate stiffness, which were related to cancer progression and metastasis such as cell proliferation, cell migration and adhesion, and angiogenesis, several orthogonal techniques were used to validate protein dysregulation between the secretome of cells grown on 2 and 47 kPa gels (mimicking healthy tissue and advanced CRC stages, respectively).

In Silico Analysis Elucidates Protein Secretion Pathways—First, to verify that the dysregulated secretome proteins were not experimental artifacts, we used SecretomeP for an *in silico* analysis to determine the cellular pathways involved in their secretion. This tool estimates the probability that a protein is secreted based on its post-translational modifications and cellular localization. Out of the 1476 proteins dysregulated between 2 versus 47 kPa conditions, 407 were predicted to be secreted, but only 113 contained a signal peptide for the classical secretory route, indicating that most of the dysregulated proteins were released into the extracellular environment via alternative pathways (Fig. 2*E* and Supplemental Table S6). Additionally, the analysis with ExoCarta, a database of proteins identified in exosomes from multiple organisms, revealed that 189 proteins can be secreted through exosomes, 68 of which have been associated with colorectal cancer cells. Experimentally, our analysis is supported by previous studies, which identified some of these proteins on the cell surface or in the secretome of KM12 cells, suggesting that they can indeed be released by cleavage or secretion (60, 61).

Dot Blot Analyses Complement and Validate Proteomics Results—12 proteins were selected for validation based on a combination of statistical significance, biological relevance, and technical feasibility. We focused on the highest dysregulated secretome proteins between soft versus stiff hydrogel and glass (FDR $\leq$0.05). Within this group, we prioritized candidates functionally linked to stiffness-responsive processes, such as cell adhesion, ECM remodeling, inflammation, and CRC progression (29–31, 61, 62). Finally, we restricted the panel to proteins for which validated antibodies were available commercially. These comprised three upregulated (COTL1, CSTB, and TXNDC17) and nine downregulated proteins (RASA1, THBS1, COL5A1/COL5A2,

expression of the 12 dysregulated secretome proteins selected for validation normalized to the mean row intensity. While 13 dysregulated proteins are shown in the heatmap, COL5A1 and COL5A2 were taken together in our validation assays, as the antibody used binds to all three COL5 isoforms.

EMILIN1, NCAM1, PAK1, NEO1, COL2A1, and ECM1). Notably, all selected proteins except ECM1 and COTL1 were predicted to follow nonclassical secretion pathways (SecretomeP score <0.6), thereby representing both conventional and unconventional secretion routes potentially modulated by matrix stiffness.

Unsupervised cluster analysis showed significant dysregulation of all 12 secretome proteins in 2 kPa gels compared to the other stiffnesses (Fig. 2*F*). Remarkably, in the hierarchical cluster analysis of the 6 dysregulated proteins of the cell extracts, the 2 kPa condition was separated from other stiffnesses, but replicates of different stiff conditions clustered randomly (Supplemental Fig. S5*E*).

Then, to support and validate the TMT-based proteomic results, we further investigated the secretome dysregulation by dot blot, cytokine arrays, and ELISA tests. Dysregulation of the 12 selected secretome proteins was analyzed by dot blot analysis (Fig. 3*A* and Supplemental Fig. S8). The initial biological replicates (KM12L4a R1-3) were analyzed to validate the TMT data, and three additional replicates (KM12L4a R4-6) were included to confirm the reproducibility of our results. Protein dysregulation between stiffer (47 kPa) and softer (2 kPa) conditions matched LC-MS/MS results for 10 of the selected proteins (COTL1, CSTB, RASA1, PAK1, EMILIN1, THBS1, COL2A1, COL5, ECM1, and NCAM), although some replicates showed nonsignificant trends and large error intervals. The other two selected proteins, TXNDC17 and NEO1, showed conflicting dysregulation trends between the original and additional replicates –TXNDC17 upregulation was observed only in the original replicates (R1-3), while NEO1 downregulation was seen in the additional replicates (R4-6)– making it challenging to draw conclusions for these two proteins.

Additionally, to explore the interplay between metastatic potential and substrate stiffness, we also extended the dot blot assays to the analysis of the secretome of two biological replicates of the poorly metastatic KM12C cells (KM12C R1-2) (Fig. 3*A* and Supplemental Fig. S8). Interestingly, all selected proteins followed the same trend as the original KM12L4a replicates, except COTL1, COL5, and NCAM. Notably, unlike the ambiguous results of the KM12L4a replicates, the poorly metastatic replicates (KM12C R1-2) confirmed the downregulation of NEO1, as expected from the LC-MS/MS findings. Overall, the dysregulation observed in LC-MS/MS was validated for most of the selected proteins, with additional replicates from the highly metastatic KM12L4a and poorly metastatic KM12C generally showing consistent results, suggesting stiffness induces important changes in the secretion of proteins.

Taken together, dot blot analyses confirmed that matrix stiffness induces reproducible and biologically meaningful alterations in the CRC secretome. The 12 validated proteins showed consistency with proteomics data, particularly those linked to cell adhesion, ECM remodeling, and tumor progression. Although some variability was observed across replicates, likely due to biological heterogeneity and technical constraints inherent to dot blot assays (*e.g.,* limited dynamic range and antibody-dependent sensitivity), most targets –including COTL1, CSTB, RASA1, THBS1, COL5, ECM1, and NCAM– consistently displayed the expected dysregulation trends across independent experiments. These results reinforce the robustness of the secretome alterations detected by quantitative proteomics and support the biological significance of stiffness-dependent changes in protein secretion in CRC.

Extending Proteomics Analysis by Investigating Cytokines— Cytokines, essential for cellular communication, are difficult to detect via LC-MS/MS due to their small size and low abundance in the secretome. To overcome this limitation, we extended the TMT-based proteomic findings to confirm the dysregulation of proteins in the secretome by an orthogonal approach and evaluate the expression levels of 80 human cytokines using a cytokine antibody microarray. We compared the softer (2 kPa) and stiffer (47 kPa) conditions in the three original KM12L4a replicates (KM12L4a R1-3). In the secretomes obtained from stiffer conditions, three cytokines were significantly upregulated (TNFα, GCP-2, and GDNF) and three were significantly downregulated (GRO, IL-8, and GROα, Fig. 3*B* and Supplemental Fig. S9, *A*–*C*). VEGF and OPG appeared to be up- and downregulated, respectively, but these changes were not statistically significant.

The results from the cytokine array were validated by ELISA on selected cytokines: one upregulated (VEGF) and three downregulated (GROα, OPG, and IL-8). These tests were performed in duplicate on the six KM12L4a biological replicates (KM12L4a R1-6) and on both KM12C biological replicates (KM12C R1-2) (Fig. 3*C*). While some comparisons between stiffer and softer conditions were not significant due to the sample size, GROα and IL-8 were consistently downregulated for all replicates, in line with the cytokine array. ELISA tests for VEGF and OPG, which showed nonsignificant differences in the cytokine arrays, confirmed nonsignificant changes for VEGF (for KM12L4a R1-3), but revealed significant changes in OPG across the KM12L4a replicates (KM12L4a R1-6). Notably, IL-8, OPG, and GROα trends were consistent across highly metastatic (KM12L4a R1-6) and poorly metastatic (KM12C R1-2) cells, but VEGF showed the opposite trend between KM12L4a R1-3 (upregulated) and the other replicates (KM12L4a R4-6 and KM12C R1-2, downregulated).

Despite their low abundance, nine of the tested cytokines were successfully identified by LC-MS/MS (Supplemental Fig. S9, *B*, *C*, and *E*). Four cytokines (VEGF, IGFBP-2, OPG, and TIMP-2) exhibited consistent trends across both methods, although not all differences reached statistical

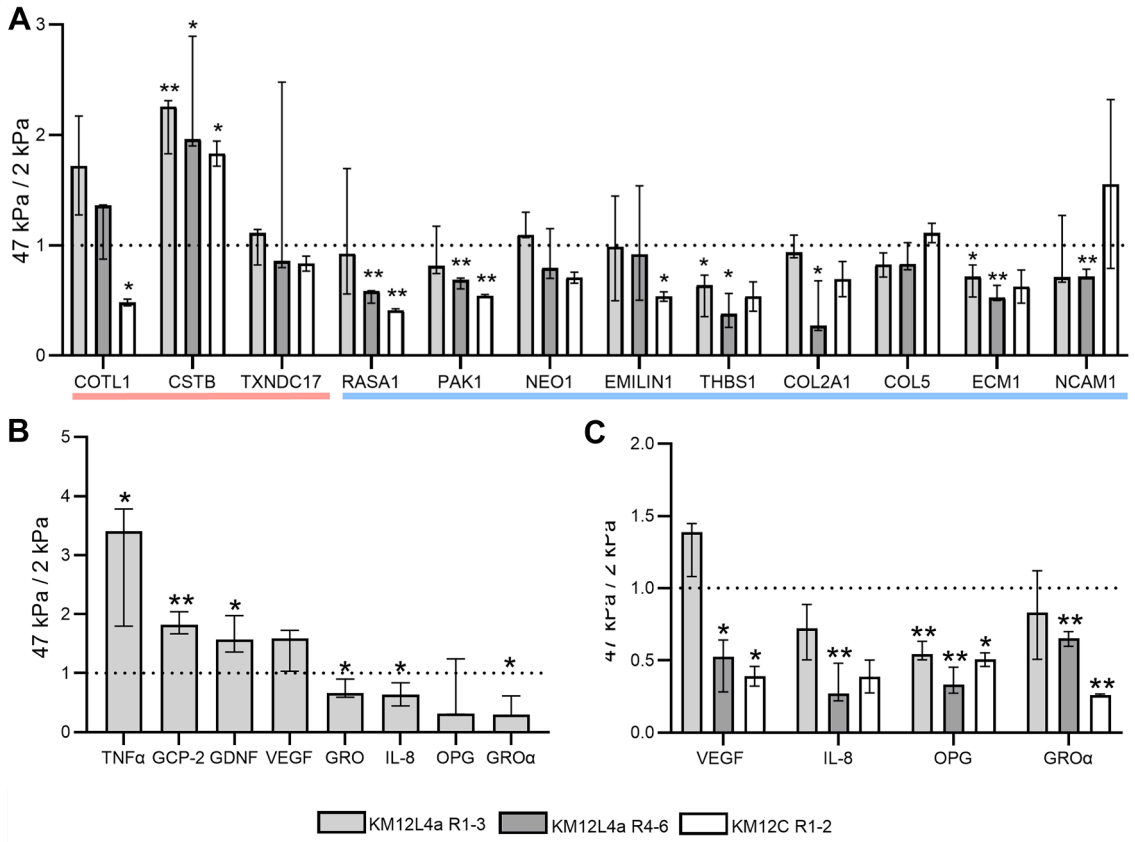

FIG. 3. **Validating and extending secretome dysregulation analysis for stiffer (47 kPa) *versus* softer (2 kPa) conditions.** *A*, dot blot analysis of selected proteins found upregulated (*red line*) and downregulated (*blue line*) in LC-MS/MS analysis. Full dataset is shown in Supplemental Fig. S8. *B* and *C*, cytokine analyses. *B*, cytokine array analysis showing upregulated and downregulated cytokines. The dataset is shown in Supplemental Fig. S9. *C*, ELISA tests for 4 selected cytokines. Data was averaged over two technical replicates. *A* and *C*, the bar represents median with 95% confidence interval. "R" denotes "replicate", showing original KM12L4a replicates (R1-3), additional replicates (R4-6), and poorly metastatic KM12C replicates (R1-2). Significance levels: (*) $p \leq 0.05$; (**) $p \leq 0.01$.

significance. For another group (angiogenin, IGFBP-3, IGFBP-4, and TIMP-1), variability among replicates limited definitive interpretation. Interestingly, TGF-β1 showed divergent patterns, being upregulated in cytokine arrays and downregulated in LC-MS/MS, which may reflect method-specific sensitivities or biological complexity.

Analyzing Functional Effects of Altered Secretome

Our analysis identified a dysregulation in several secreted factors that can influence or regulate key cellular processes, including inflammation (*e.g.,* GRO-family, interleukin 8), cell growth and apoptosis (*e.g.,* TGFβ-family), cell migration and metastasis (*e.g.,* GCP2, GDNF), angiogenesis (*e.g.,* VEGF, ANG, THBS1), and matrix remodeling (MMPs). Understanding how stiffness-dependent dysregulated secreted factors identified by TMT-based and cytokine antibody microarrays-based proteomics regulate these processes is critical to elucidate mechanobiological drivers of cancer progression and metastasis according to the stiffness. Therefore, we next focused on validating the impact on these processes of the different secretomes collected from cells grown on softer substrates (2 kPa) and on stiffer substrates (47 kPa).

Effects on Cell Migration—Deciphering the proteomic signals underlying cancer cell migration is essential to understand the mechanisms driving tumor invasion and metastatic progression. Given the differential regulation of proteins involved in adhesion and motility observed in our secretome profiling, we investigated how these secreted factors affect migratory behavior of cancer cells.

Therefore, functional validation using wound healing assays confirmed that the secretome from highly metastatic KM12L4a cells modulates the migration of poorly metastatic KM12C cells according to the stiffness of the substrate (Fig. 4*A*). Notably, the secretome from KM12L4a cells grown on soft matrices (2 kPa) increased KM12C migration speed in about 3-fold compared to control (lyophilized starvation medium), while the secretome from cells on stiff substrates (47 kPa) induced an about 1.5-fold increase. These findings

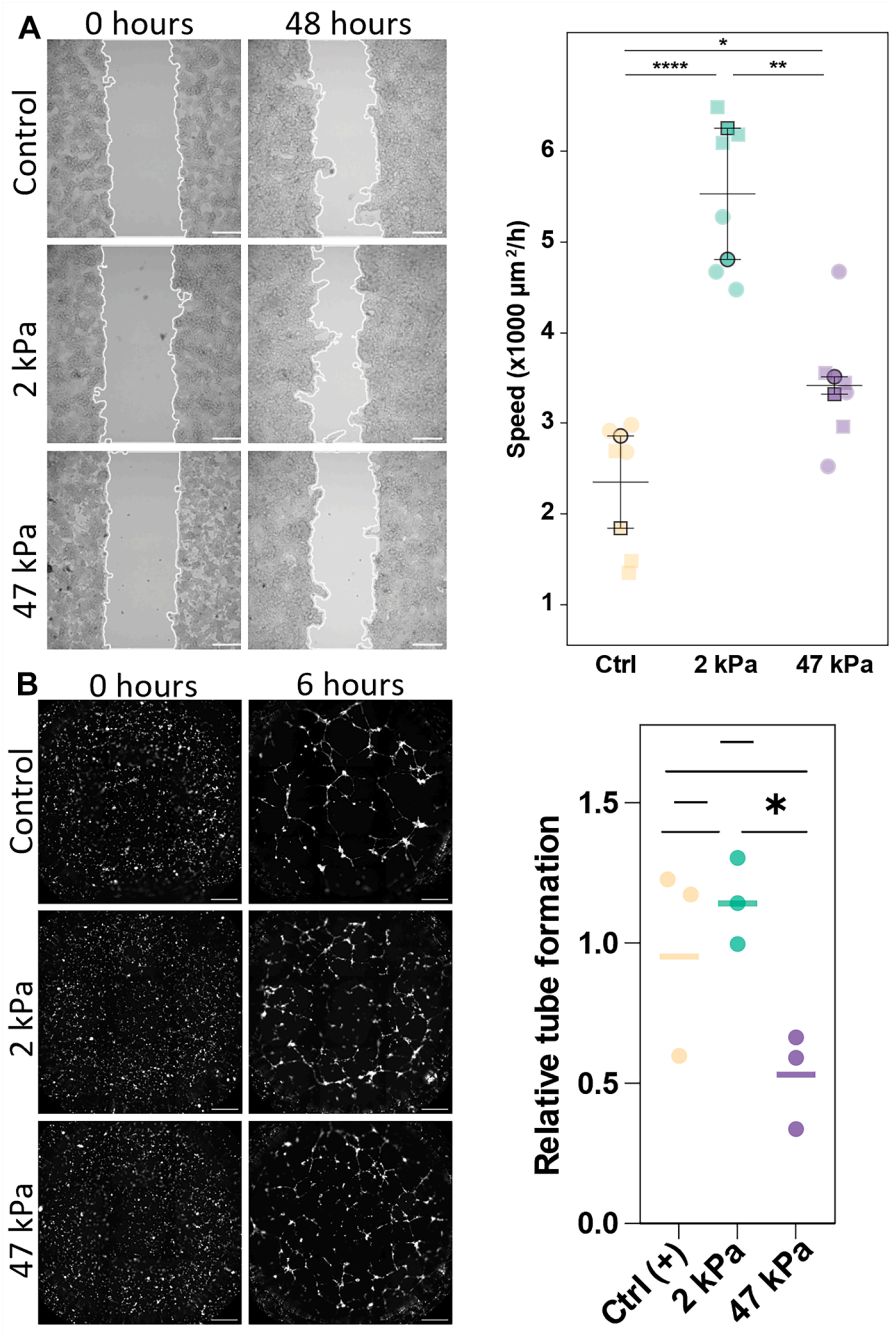

FIG. 4. **Analyzing functional effects of secretome on cell migration and angiogenesis.** *A*, cell migration assay for KM12C wound healing assays incubated with control (lyophilized starvation medium), softer (2 kPa), and stiffer (47 kPa) lyophilized secretomes at different timepoints. Representative images with 200 µm scale bars are shown. Quantified data was obtained from minimally two different replicate samples, from three regions per sample. *B*, angiogenesis tube formation assays for Human Umbilical Vein Endothelial (HUVEC) cells tube formation incubated with control (positive control with complete medium showing maximum tube formation potential), softer (2 kPa), and stiffer (47 kPa) lyophilized secretomes at different timepoints. Representative images with 500 µm scale bars. Quantified data shows the increment of the normalized cell area through time that was normalized to the median of the control condition. Data was obtained from three different replicate samples. *A and B*, significance levels: (–) $p > 0.05$, non-significant; (*) $p \leq 0.05$; (**) $p \leq 0.01$; (****) $p \leq 0.0001$.

support the existence of a stiffness-sensitive, secretome-driven mechanism enhancing migratory potential, consistent with the proteomic alterations detected.

Effects on Angiogenesis—Angiogenesis is a hallmark of cancer progression, providing solid tumors with the vascular support required for sustained tumor growth, nutrient

delivery, and metastatic dissemination, while removing simultaneously waste products.

Given the dysregulation of angiogenesis-related proteins identified in our secretome analysis, we next investigated whether stiffness-dependent secreted factors could modulate endothelial cell behavior. Functional angiogenesis assays demonstrated that the secretome from highly metastatic KM12L4a cells cultured on soft substrates (2 kPa) was nearly twice as effective in promoting blood vessel formation compared to the secretome from cells grown on stiff substrates (47 kPa). Remarkably, the pro-angiogenic effect of the soft-matrix-derived secretome approached that of the positive control (complete medium), highlighting its potent stimulatory capacity (Fig. 4*B*). Similar results were obtained when applying the secretome of poorly metastatic KM12C cells (Supplemental Fig. S10*A*). These findings suggest that matrix stiffness modulates the angiogenic potential of the tumor secretome, in agreement with the proteomic alterations observed, and that this mechanism may be independent of the metastatic potential of the cells in the KM12 model.

Effects on ECM Production and Degradation—The dynamic remodeling of the ECM is a critical component of solid tumor progression, influencing tissue architecture, cell signaling, and metastatic potential. Tumor cells not only respond to ECM changes but also actively reshape their microenvironment by producing, modifying, and degrading ECM components.

Proteomic profiling revealed an enrichment of ECM-related proteins—including COL2A1, COL5A1, and COL6A3—in the secretome of KM12L4a cells cultured on soft substrates. Then, to further investigate this observation, we analyzed the expression and intracellular distribution of these three collagen isoforms (Fig. 5, *A* and *C*i, and Supplemental Fig. S11). While COL5A1 and COL6A3 exhibited similar patterns across softer and stiffer substrate conditions, COL2A1 showed significantly increased intracellular retention in cells on stiff substrates. This may reflect reduced secretion or altered trafficking of collagen 2A1 under high-stiffness conditions, resulting in intracellular accumulation. The expected increase in secreted collagen on softer substrates was not observed, possibly due to the removal of loosely attached extracellular collagen during the immunolabeling process.

To complement these findings, we evaluated the effect of secretome on ECM degradation, a process often mediated by colorectal CAFs in the tumor microenvironment. Using fluorescently labeled gelatin-coated coverslips, we assessed the effect of the secretome on gelatin degradation by CAFs (Fig. 5, *B* and *C*ii). Secretomes from different stiffness conditions showed no significant differences, possibly because the cells produced their own ECM over time, which may have masked any secretome-driven changes. However, secretomes harvested from both softer and stiffer conditions differed significantly from the control (lyophilized starvation medium). Notably, KM12 cells did not display intrinsic matrix-degrading activity (Supplemental Fig. S10*B*), demonstrating that the observed effects arise from secretome-driven modulation of CAF function, not from direct tumor-cell proteolysis factors. These results suggest that, despite possible masking effects, the secretome –modulated by substrate stiffness– can influence ECM remodeling activity through paracrine cues, in line with the differential proteomic signatures observed.

Collectively, these results demonstrate that stiffness-induced protein dysregulation in the secretome of CRC cells can orchestrate critical pro-metastatic processes in CRC. Our proteomics data reveal a consistent enrichment of secreted factors involved in cell migration, angiogenesis, and extracellular matrix remodeling under soft-substrate conditions—features functionally validated through *in vitro* assays. This secretome reprogramming, modulated by the mechanical properties of the microenvironment, reflects an adaptive strategy by which tumor cells fine-tune their external signaling landscape to promote invasion and cancer progression. Given that increased tissue stiffness is a hallmark of tumor evolution in CRC patients, these findings underscore the importance of considering biomechanical cues as regulators of secretory phenotypes. Beyond their mechanistic significance, our results suggest that the stiffness-responsive secretome may offer novel biomarker candidates or therapeutic targets for disrupting the metastatic cascade in CRC.

DISCUSSION

In this study, we explore how ECM mechanical properties influence CRC, focusing on protein expression changes in response to the stiffer environments observed during tumor progression. Our findings show that the highly metastatic KM12L4a CRC cells are mechanosensitive, with their morphology changing with substrate stiffness, making them suitable for studying the impact of altered ECM stiffness.

Despite changes in cell morphology, our in-depth proteomic analysis revealed that substrate stiffnesses above 2 kPa do not alter global intracellular protein expression in KM12L4a cells. Other proteomic studies on liver cancer and endothelial cells reported significant stiffness-related effects, with 240 to 350 dysregulated intracellular proteins (for a similar total protein count), but comparisons across systems remain challenging due to differences in cell lines, ECM ranges, and experimental designs (17, 19). In CRC, other factors have been shown to impact intracellular protein expression. For example, 566 proteins were dysregulated when comparing adenoma and adenocarcinoma tissue samples from CRC patients to healthy tissue, reflecting the effect of CRC progression, and 1318 proteins were dysregulated in the KM12 cell model, indicating the influence of the metastatic potential (30, 31, 62). While stiffness did not significantly impact intracellular protein abundance in our system, the robustness of our proteomic analysis is supported by the high number of proteins quantified and the consistency of findings with parallel secretome analyses among the three biological

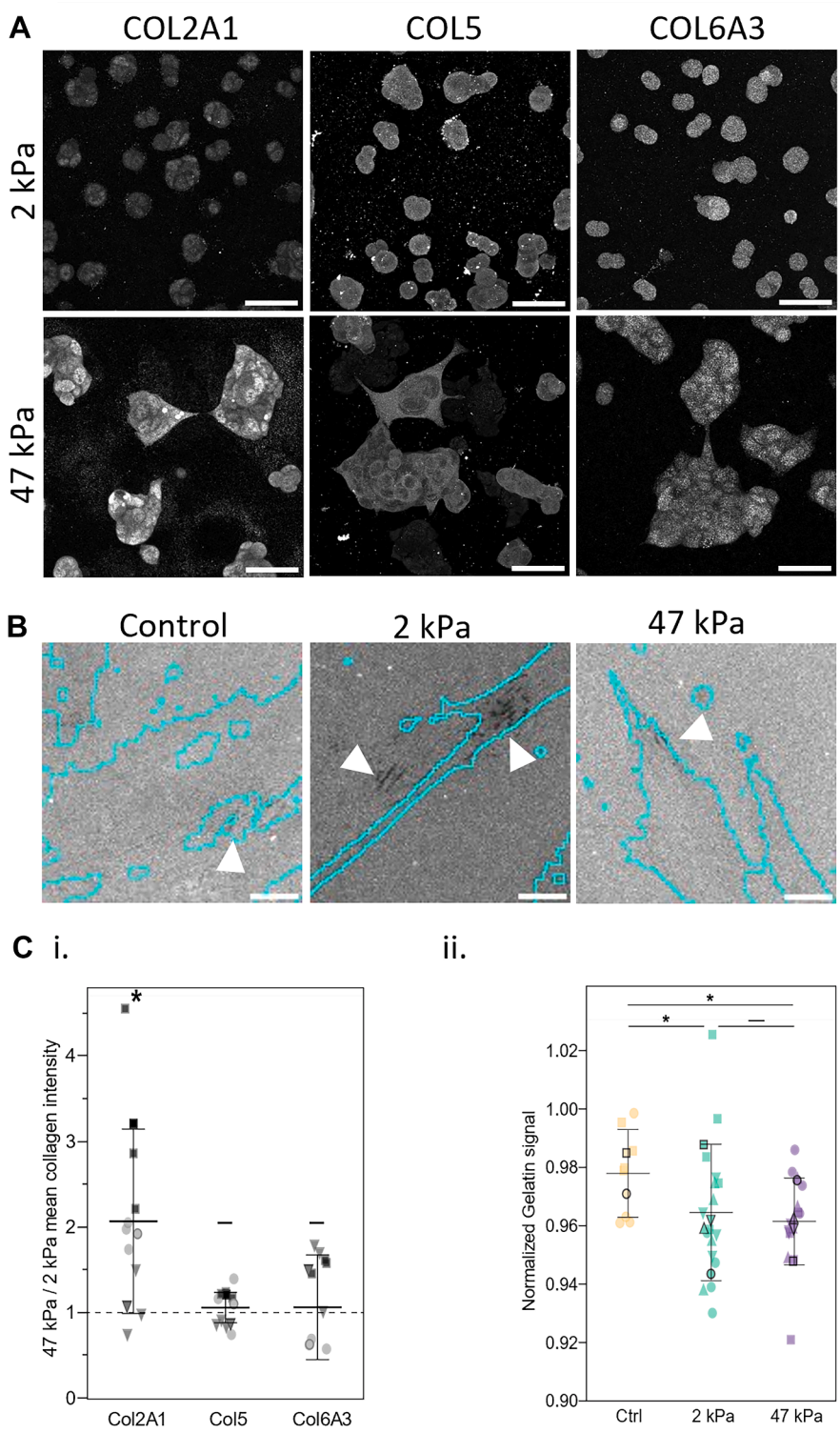

FIG. 5. **Analyzing functional effects of secretome on ECM production and degradation for stiffer (47 kPa) versus softer (2 kPa) conditions.** *A*, collagen protein expression. Representative images for the maximum z-projection of immunolabeled collagens for KM12L4a cells grown on top of softer (2 kPa) and stiffer (47 kPa) substrates. Side-by-side images were taken with the same acquisition and display settings. Figure shows representative images of three biological replicates, with three fields of view imaged per replicate. The full dataset is available in Supplemental Fig. S11. The scale bar represents: 50 μm. *B*, gelatin degradation assay. Representative images of CAF cells (*blue lines* show segmented cell boundary) incubated with different lyophilized secretomes to assess the effect on gelatin degradation. *Arrows*

replicates per condition. Importantly, we acknowledge that protein stability does not exclude other types of regulation, such as changes in protein localization or organization. Indeed, previous spatial proteomic studies and our own tubulin and actin data support this, showing morphological alterations without corresponding changes in total protein levels. In fact, previous spatial proteomic studies have demonstrated that many dysregulated proteins shift in localization, and our tubulin analysis shows unchanged global expression levels despite evident changes in cell morphology and cytoskeletal structure (30, 31).

The absence of substantial stiffness-dependent changes in the intracellular proteome are, at first sight, unexpected. Other studies with alternative CRC models (HCT116 and SW480 cells) have revealed stiffness-responsive transcriptional programs, including HSF4-driven rewiring, indicating that mechanotransduction can produce strong transcriptional outputs (63). Several factors may explain why KM12L4a cells show clear mechanosensitive phenotypes and extensive secretome remodeling but limited intracellular proteomic changes. First, prolonged serum starvation may uncouple transcription and translation, attenuating stiffness-dependent proteomic responses, while still allowing changes in secretion. Second, KM12 cells may possess intrinsic buffering mechanisms involving post-transcriptional, translational, or related to protein turnover, that dampen intracellular proteomic changes despite upstream transcriptional or mechanical cues. Third, transcriptome-proteome mismatches are common, especially under nutrient-limiting conditions, and may obscure transient or low-amplitude proteomic effects (64, 65). Together, these factors provide a plausible explanation for the apparent discrepancy between strong phenotypic and secretome responses, and the muted intracellular proteomic changes observed here.

In contrast, the secretome showed substantial responsiveness to substrate stiffness, as evidenced by LC-MS/MS and cytokine array analyses. This was further validated through orthogonal methods, including dot blot and ELISA, confirming that mechanical cues significantly alter the composition of secreted proteins. Proteomic profiling and *in silico* analyses confirm that 28% of the dysregulated secretome proteins are released via both classical and nonclassical secretion pathways. Notably, 46% of these proteins have been linked to exosomes, with 17% specifically associated with CRC. Exosomes, small extracellular vesicles (40–160 nm), transport bioactive cargo that can influence the ECM and surrounding cells (66–68). Previous reports show that substrate stiffness affects exosome composition, with stiffer substrates inducing an increase in molecules involved in cell-ECM interactions (*e.g.,* thrombospondin 1, integrins), ECM degradation (*e.g.,* MMP9), and inflammation and immune evasion (*e.g.,* S100-family) (18, 20, 21, 69, 70). These proteins classes align with our GO and Reactome analyses, which indicate that dysregulated proteins in the secretome are involved in cell migration and adhesion, intracellular transport, cell death and proliferation, and protein and RNA modifications.

Importantly, substrate stiffness appears to have a more pronounced effect on the secretome than in the metastatic potential of the cells. In our analysis, 44% of the identified proteins were dysregulated due to changes in stiffness, while only 6 to 12% were linked to metastatic potential in previous studies, including the KM12 model (60, 61). Although direct comparisons are challenging due to differences in cell lines and methodologies, the stark difference in the percentage of dysregulated proteins highlights the dominant critical role of stiffness. Additionally, the overlap in affected proteins suggests that both stiffness and metastatic potential may act together to regulate similar biological processes, potentially promoting metastasis. This is consistent with other models in different cancer types, such as breast cancer, where oncogenic mutations enhance cell sensitivity to matrix stiffness, reinforcing the interplay between these factors (21).

Analysis of the effect of the different secretomes on cell behavior shows that the secretome from metastatic cells grown on softer substrates increases the migration speed of poorly metastatic CRC cells and induces angiogenesis more effectively than secretome from cells grown on stiffer substrates. This suggests that metastasized cells, while forming metastases in relatively soft secondary organs, may enhance the migration of poorly metastatic cells at the primary tumor. The interplay between primary tumors and metastases – including micro-metastasis dormancy and reactivation, and metastatic reseeding – is increasingly recognized as integral to tumor progression and supports our hypothesis (71–73). Additionally, our angiogenesis assays suggest that metastasized cells can rapidly develop vasculature in newly colonized sites, potentially critical for supporting the rapid growth of metastases.

Our bioinformatic analyses also identified proteins associated with the extracellular matrix, prompting us to evaluate how substrate stiffness impacts collagen deposition and gelatin. Although proteomic data indicated increased ECM dynamics on softer substrates, our functional assays showed no differences (except for intracellular distribution of COL2A1). While we adhere to standardized, extended timescales to replicate *in vivo* scenarios, future research could focus on the impact of self-deposited ECM to better assess the effect of the secretome. Despite finding no clear impact of

indicate darker regions where gelatin was degraded. The scale bar represents 20 μm. *C*, *Plots show* quantification of the mean collagen intensity in regions of interest (segmented cells) (i) and normalized gelatin signal (ratio of intracellular versus extracellular gelatin signal per field of view) (ii). Significance levels: (–) $p > 0.05$, nonsignificant; (*) $p \leq 0.05$; (**) $p \leq 0.01$; (****) $p \leq 0.0001$.

stiffness, our analyses indicate that matrix deposition and degradation are stimulated by the secretome, regardless of matrix stiffness. This suggests a positive feedback loop where substrate stiffness and remodeling gradually increase during tumor progression (as previously suggested) (6, 8).

As with any serum-free secretome study, a key limitation of this study is the 48 h serum deprivation step required to avoid serum protein contamination. Although serum withdrawal can induce mild cellular stress, all conditions were treated identically, cell viability remained above 80% and we detected no autophagy activation or intracellular proteome changes across different stiffness. Previous work has shown that nutrient deprivation can modulate autophagy in a stiffness-dependent manner (74); however, this was not observed in our system. Instead, transcriptional responses to serum starvation varied by stiffness, particularly between 2 kPa and glass, suggesting that matrix rigidity influences how cells adapt to stress. These findings are in agreement with previous reports using the KM12 model, where similar serum deprivation protocols did not induce autophagy-associated signatures (30–32). Although the effects observed here were modest and did not translate into autophagy-driven proteomic changes, we cannot fully exclude the possibility that serum deprivation induced low-level activation of nonclassical secretory routes in a subset of proteins, as previously described in mechanotransduction–autophagy crosstalk (74). A second limitation of the study is that we did not perform vesicle-specific proteomics. Although our findings align with previous reports showing that increased matrix stiffness enhances exosome secretion through mechanotransduction pathways such as Akt–Rab8 and p53–thioredoxin signaling (21, 75), isolating vesicular subproteomes would provide deeper insight into how ECM mechanics regulate secretory routes and intercellular communication and will be an important focus of future studies. Finally, we also acknowledge that annotation-based bioinformatic tools (STRING, Reactome, GO) rely on curated datasets and can introduce biases toward well-studied proteins, potentially underrepresenting novel or less-characterized ones.

In summary, our study highlights the central role of secretome-mediated, stiffness-induced proteomic reprogramming in CRC. This is the first comprehensive proteomic analysis to evaluate the full spectrum of secreted proteins in response to mechanical cues, extending beyond exosomal content to the broader secretome landscape. These findings establish a foundation for future studies on the interplay between mechanotransduction, ECM dynamics, and secretory phenotypes, and point to new avenues for therapeutic targeting of the tumor microenvironment.

DATA AVAILABILITY

The mass spectrometry proteomics data have been deposited at the ProteomeXchange Consortium via the PRIDE partner repository with the data set identifier PXD064023.

SIGNIFICANCE STATEMENT

Although tumor stiffness is a hallmark of cancer progression, its influence on protein expression remains poorly understood. Our study reveals that increased matrix stiffness, a key feature of colorectal cancer tumors, alters the secreted protein profile (secretome) without significantly impacting the expression of intracellular proteins. These stiffness-driven secretome changes enhance cell migration, angiogenesis, and matrix remodeling, all of which contribute to a more aggressive tumor behavior. This work highlights a critical mechanism where the physical properties of the tumor microenvironment drive cancer progression. By linking biomechanical forces to functional proteomic changes, our findings open new avenues for considering therapeutic strategies to target tumor stiffness in metastasis, the leading cause of cancer mortality.

Supplemental data—This article contains supplemental data (29, 34–38, 40, 44, 46–49, 53, 56, 57, 61, 76–82).

Acknowledgments—We thank Fidler's lab (MD Anderson Cancer Center) for sharing KM12 model cell lines, De Wever's lab (UGent) for sharing the CAF CT5.3 cell line, and Prof. E. Planus for sharing details regarding the gelatin degradation protocol. The support of the Advanced Optic Microscopy Unit of the Instituto de Salud Carlos III is gratefully acknowledged.

Funding and additional information—This work was performed with the financial support of PID2022 to -140307OB-I00 funded by MCIN/AEI/10.13039/501100011033 and by "ERDF A way of making Europe" to R. B., PI20CIII/00019 and PI23CIII/00027 grants from the AES-ISCIII program, co-financed with FEDER funds, to R. B. Additionally, this project has received funding to R. B. from the EIC Pathfinder program 2023 of the European Innovation Council (EIC) under Grant Agreement #101130574. Additionally, S. R. gratefully acknowledges KU Leuven financial support through internal funds (IDN/20/021, KA/20/026, C14/22/085). This work was also funded by the Research Foundation Flanders (FWO) through a project with grant number G0C2422N. In addition, C. C. and S. A. are recipients of an FWO PhD fellowship for fundamental research, grant numbers 1121223N and 1S95123N. G.S.-F. is recipient of an FWO junior postdoctoral fellowship, grant number 12AML24N. C. C. received an FWO travel grant for a long stay abroad.

Author contributions—C. C., A. M. C., G. S. F., B. S., L. G., S. A., P. H. J. K., R. B., and S. R. writing–review and editing; C. C., A. M. C., G. S. F., R. B., and S. R. writing–original draft; C. C., A. M. C., G. S. F., R. B., and S. R. visualization; C. C.,

A. M. C., G. S. F., R. B., and S. R. validation; C. C., A. M. C., G. S. F., B. S., L. G., and S. A. methodology; C. C., A. M. C., G. S. F., and R. B. investigation; C. C., G. S. F., S. A., R. B., and S. R. funding acquisition; C. C., A. M. C., and G. S. F. formal analysis; C. C., A. M. C., G. S. F., R. B., and S. R. data curation; C. C., A. M. C., G. S. F. R. B., and S. R. conceptualization; P. H. J. K., R. B., and S. R. supervision; P. H. J. K., R. B., and S. R. resources; P. H. J. K., R. B., and S. R. project administration.

Conflict of interest—The authors declare no competing interests.

Abbreviations—The abbreviations used are: CRC, colorectal cancer; DAPI, 6-diamidino-2-Phenylindole; DDA, data-dependent acquisition; dH2O, distilled water; DMEM, Dulbecco's modified Eagle medium; D-PBS, Dulbecco's phosphate-buffered saline; EBM-2, endothelial cell basal medium; ECM, extracellular matrix; FBS, fetal bovine serum; FDR, false discovery rate; GO, gene ontology; HUVEC, human umbilical vein endothelial cell; MMP, matrix metalloproteinase; OPG, osteoprotegerin; TIMP, tissue inhibitor of metalloproteinase; TMT, Tandem Mass Tag; VEGF, vascular endothelial growth factor.

Received June 28, 2025, and in revised form, January 12, 2026
Published, MCPRO Papers in Press, January 23, 2026, https://doi.org/10.1016/j.mcpro.2026.101515

REFERENCES

1. Rodriguez-Salas, N., Dominguez, G., Barderas, R., Mendiola, M., García-Albéniz, X., Maurel, J., *et al*. (2017) Clinical relevance of colorectal cancer molecular subtypes. *Crit. Rev. Oncol. Hematol.* **109**, 9–19
2. Dillekås, H., Rogers, M. S., and Straume, O. (2019) Are 90% of deaths from cancer caused by metastases? *Cancer Med.* **8**, 5574–5576
3. Dunne, P. D., and Arends, M. J. (2024) Molecular pathological classification of colorectal cancer—an update. *Virchows Archiv.* **484**, 273–285
4. Holleczek, B., Rossi, S., Domenic, A., Innos, K., Minicozzi, P., Francisci, S., *et al*. (2015) On-going improvement and persistent differences in the survival for patients with colon and rectum cancer across Europe 1999-2007 - results from the EUROCARE-5 study. *Eur. J. Cancer* **51**, 2158–2168
5. Hanahan, D. (2022) Hallmarks of cancer: new dimensions. *Cancer Discov.* **12**, 31–46
6. Ishihara, S., and Haga, H. (2022) Matrix stiffness contributes to cancer progression by regulating transcription factors. *Cancers (Basel)* **14**. https://doi.org/10.3390/cancers14041049
7. Kawano, S., Kojima, M., Higuchi, Y., Sugimoto, M., Ikeda, K., Sakuyama, N., *et al*. (2015) Assessment of elasticity of colorectal cancer tissue, clinical utility, pathological and phenotypical relevance. *Cancer Sci.* **106**, 1232–1239
8. Simi, A. K., Pang, M., and Nelson, C. M. (2018) Extracellular matrix stiffness exists in a feedback loop that drives tumor progression. *Adv. Exp. Med. Biol.* **1092**, 57–67
9. Nissen, N. I., Karsdal, M., and Willumsen, N. (2019) Collagens and cancer associated fibroblasts in the reactive stroma and its relation to cancer biology. *J. Exp. Clin. Cancer Res.* **38**, 1–12
10. Belhabib, I., Zaghdoudi, S., Lac, C., Bousquet, C., and Jean, C. (2021) Extracellular matrices and cancer-associated fibroblasts: targets for cancer diagnosis and therapy? *Cancers (Basel)* **13**. https://doi.org/10.3390/cancers13143466
11. Niland, S., and Eble, J. A. (2021) Hold on or cut? Integrin- and MMP-mediated cell-matrix interactions in the tumor microenvironment. *Int. J. Mol. Sci.* **22**, 1–42
12. Escolano, J. C., Taubenberger, A. V., Abuhattum, S., Schweitzer, C., Farrukh, A., del Campo, A., *et al*. (2021) Compliant substrates enhance macrophage cytokine release and NLRP3 inflammasome formation during their pro-inflammatory response. *Front. Cell Dev. Biol.* **9**, 1–14
13. Blokland, K. E. C., Nizamoglu, M., Habibie, H., Borghuis, T., Schuliga, M., Melgert, B. N., *et al*. (2022) Substrate stiffness engineered to replicate disease conditions influence senescence and fibrotic responses in primary lung fibroblasts. *Front. Pharmacol.* **13**, 1–17
14. Wei, J., Yao, J., Yan, M., Xie, Y., Liu, P., Mao, Y., *et al*. (2022) The role of matrix stiffness in cancer stromal cell fate and targeting therapeutic strategies. *Acta Biomater.* **150**, 34–47
15. Su, J. X., Li, S., Jia, Z., feng, X., Zhang, Z. J., Yan, Y., *et al*. (2023) Chemotherapy-induced metastasis: molecular mechanisms and clinical therapies. *Acta Pharmacol. Sin.* **44**, 1725–1736
16. Hou, S., Zhao, Y., Chen, J., Lin, Y., and Qi, X. (2024) Tumor-associated macrophages in colorectal cancer metastasis: molecular insights and translational perspectives. *J. Transl. Med.* **22**, 1–14
17. Reid, S. E., Kay, E. J., Neilson, L. J., Henze, A., Serneels, J., McGhee, E. J., *et al*. (2017) Tumor matrix stiffness promotes metastatic cancer cell interaction with the endothelium. *EMBO J.* **36**, 2373–2389
18. Patwardhan, S., Mahadik, P., Shetty, O., and Sen, S. (2021) ECM stiffness-tuned exosomes drive breast cancer motility through thrombospondin-1. *Biomaterials* **279**, 121185
19. Gao, X., Qian, J., Zhang, Y., Wang, H., Cui, J., and Yang, Y. (2023) Analysis of differential membrane proteins related to matrix stiffness-mediated metformin resistance in hepatocellular carcinoma cells. *Proteome Sci.* **21**, 1–15
20. Sneider, A., Liu, Y., Starich, B., Du, W., Nair, P. R., Marar, C., *et al*. (2024) Small extracellular vesicles promote stiffness-mediated metastasis. *Cancer Res. Commun.* **4**, 1240–1252
21. Wu, B., Liu, D. A., Guan, L., Myint, P. K., Chin, L. K., Dang, H., *et al*. (2023) Stiff matrix induces exosome secretion to promote tumour growth. *Nat. Cell Biol.* **25**, 415–424
22. Morikawa, K., Walker, S. M., Jessup, J. M., and Fidler, I. (1988) *In vivo* selection of highly metastatic cells from surgical specimens of different primary human colon carcinomas implanted into nude mice. *Cancer Res.* **48**, 1943–1948
23. Morikawa, K., Walker, S. M., Nakajima, M., Pathak, S., Jessup, J. M., and Fidler, I. (1988) Influence of organ environment on the growth, selection, and metastasis of human colon carcinoma cells in nude mice. *Cancer Res.* **48**, 6863–6871
24. Hegde, P., Qi, R., Gaspard, R., Abernathy, K., Dharap, S., Earle-Hughes, J., *et al*. (2001) Identification of tumor markers in models of human colorectal cancer using a 19,200-element complementary DNA microarray. *Cancer Res.* **61**, 7792–7797
25. Kuniyasu, H., Ohmori, H., Sasaki, T., Sasahira, T., Yoshida, K., Kitadai, Y., *et al*. (2003) Production of interleukin 15 by human Colon cancer cells is associated with induction of Mucosal Hyperplasia, angiogenesis, and metastasis. *Clin. Cancer Res.* **9**, 4802–4810
26. Li, Q., Lau, A., Morris, T. J., Guo, L., Fordyce, C. B., and Stanley, E. F. (2004) A syntaxin 1, Gαo, and N-Type calcium channel complex at a presynaptic nerve terminal: analysis by quantitative immunocolocalization. *J. Neurosci.* **24**, 4070–4081
27. Calon, A., Espinet, E., Palomo-Ponce, S., Tauriello, D. V. F., Iglesias, M., Céspedes, M. V., *et al*. (2012) Dependency of colorectal cancer on a TGF-β-Driven program in stromal cells for metastasis initiation. *Cancer Cell* **22**, 571–584
28. Montero-Calle, A., Gómez de Cedrón, M., Quijada-Freire, A., Solís-Fernández, G., López-Alonso, V., Espinosa-Salinas, I., *et al*. (2022) Metabolic reprogramming helps to define different metastatic tropisms in colorectal cancer. *Front. Oncol.* **12**, 1–19
29. Solís-Fernández, G., Montero-Calle, A., Sánchez-Martínez, M., Peláez-García, A., Fernández-Aceñero, M. J., Pallarés, P., *et al*. (2022) Aryl hydrocarbon receptor-interacting protein regulates tumorigenic and metastatic properties of colorectal cancer cells driving liver metastasis. *Br. J. Cancer* **136**, 1604–1615
30. Mendes, M., Peláez-García, A., López-Lucendo, M., Bartolomé, R. A., Calviño, E., Barderas, R., *et al*. (2017) Mapping the spatial proteome of metastatic cells in colorectal cancer. *Proteomics* **17**, 1–11
31. Solís-Fernández, G., Montero-Calle, A., Martínez-Useros, J., López-Janeiro, Á., Ríos, V. D. L., Sanz, R., *et al*. (2022) Spatial proteomic

analysis of isogenic metastatic colorectal cancer cells reveals key dysregulated proteins associated with lymph node, liver, and lung metastasis. *Cells* **11**, 1–23
32. Barderas, R., Bartolomé, R. A., Fernandez-Aceñero, M. J., Torres, S., and Casal, J. I. (2012) High expression of IL-13 receptor α2 in colorectal cancer is associated with invasion, liver metastasis, and poor prognosis. *Cancer Res.* **72**, 2780–2790
33. Zheng, Y., Zhou, R., Cai, J., Yang, N., Wen, Z., Zhang, Z., *et al*. (2023) Matrix stiffness triggers lipid metabolic cross-talk between tumor and stromal cells to mediate Bevacizumab resistance in colorectal cancer liver metastases. *Cancer Res.* **83**, 3577–3592
34. Shi, X., and Janmey, P. A. (2023) Large polyacrylamide hydrogels for large-batch cell culture and mechanobiological studies. *Macromol Biosci.* **23**, 1–8
35. [preprint] Cresens, C., Aytekin, S., Shaghaghi, B., Gerrits, L., Montero-Calle, A., Barderas, R., *et al*. (2024) Synthesis and mechanical characterization of polyacrylamide (PAAm) hydrogels with different stiffnesses for large-batch cell culture applications. *bioRxiv*. https://doi.org/10.1101/2024.09.17.613503
36. Syed, S., Karadaghy, A., and Zustiak, S. (2015) Simple polyacrylamide-based multiwell stiffness assay for the study of stiffness-dependent cell responses. *J. Vis. Exp.* **2015**, 1–12
37. Caliari, S. R., and Burdick, J. A. (2016) A practical guide to hydrogels for cell culture. *Nat. Methods* **26**, 72–82
38. Stanton, A. E., Tong, X., and Yang, F. (2019) Varying solvent type modulates collagen coating and stem cell mechanotransduction on hydrogel substrates. *APL Bioeng.* **3**, 1–9
39. De Vlieghere, E., Gremonprez, F., Verset, L., Mariën, L., Jones, C. J., De Craene, B., *et al*. (2015) Tumor-environment biomimetics delay peritoneal metastasis formation by deceiving and redirecting disseminated cancer cells. *Biomaterials* **54**, 148–157
40. Van Zundert, I., Maenhoudt, N., De Vriendt, S., Vankelecom, H., Fortuni, B., and Rocha, S. (2022) Fluorescence imaging of 3D cell models with subcellular resolution. *Bio Protoc.* **12**, 1–20
41. Wisniewski, J. R., and Gaugaz, F. Z. (2015) Fast and sensitive total protein and peptide assays for proteomic analysis. *Anal Chem.* **87**, 4110–4116
42. von Mering, C., Huynen, M., Jaeggi, D., Schmidt, S., Bork, P., and Snel, B. (2003) STRING: a database of predicted functional associations between proteins. *Nucleic Acids Res.* **31**, 258–61
43. Szklarczyk, D., Nastou, K., Koutrouli, M., Kirsch, R., Mehryary, F., Hachilif, R., *et al*. (2025) The STRING database in 2025: protein networks with directionality of regulation. *Nucleic Acids Res.* **53**, D730–D737
44. Bendtsen, J. D., Jensen, L. J., Blom, N., Von Heijne, G., and Brunak, S. (2004) Feature-based prediction of non-classical and leaderless protein secretion. *Protein Eng. Des. Sel.* **17**, 349–356
45. Teufel, F., Almagro Armenteros, J. J., Johansen, A. R., Gíslason, M. H., Pihl, S. I., Tsirigos, K. D., *et al*. (2022) SignalP 6.0 predicts all five types of signal peptides using protein language models. *Nat. Biotechnol.* **40**, 1023–1025
46. Simpson, R. J., Kalra, H., and Mathivanan, S. (2012) Exocarta as a resource for exosomal research. *J. Extracell. Vesicles* **1**, 1–6
47. Mathivanan, S., and Simpson, R. J. (2009) ExoCarta: a compendium of exosomal proteins and RNA. *Proteomics* **9**, 4997–5000
48. Mathivanan, S., Fahner, C. J., Reid, G. E., and Simpson, R. J. (2012) ExoCarta 2012: database of exosomal proteins, RNA and lipids. *Nucleic Acids Res.* **40**, 1241–1244
49. Keerthikumar, S., Chisanga, D., Ariyaratne, D., Al Saffar, H., Anand, S., Zhao, K., *et al*. (2016) ExoCarta: a web-based compendium of exosomal cargo. *J. Mol. Biol.* **428**, 688–692
50. Sherman, B. T., Hao, M., Qiu, J., Jiao, X., Baseler, M. W., Lane, H. C., *et al*. (2022) DAVID: a web server for functional enrichment analysis and functional annotation of gene lists (2021 update). *Nucleic Acids Res.* **50**, W216–W221
51. Fabregat, A., Sidiropoulos, K., Viteri, G., Marin-Garcia, P., Ping, P., Stein, L., *et al*. (2018) Reactome diagram viewer: data structures and strategies to boost performance. *Bioinformatics* **34**, 1208–1214
52. Perez-Riverol, Y., Bai, J., Bandla, C., García-Seisdedos, D., Hewapathirana, S., Kamatchinathan, S., *et al*. (2022) The PRIDE database resources in 2022: a hub for mass spectrometry-based proteomics evidences. *Nucleic Acids Res.* **50**, D543–D552
53. Schneider, C. A., Rasband, W. S., and Eliceiri, K. W. (2012) NIH image to ImageJ: 25 years of image analysis. *Nat. Methods* **9**, 671–675
54. Abràmoff, M. D., Magalhães, P. J., and Ram, S. J. (2004) Image processing with imageJ. *Biophotonics Int.* **11**, 36–41
55. Casal, J. I., Fernández-aceñero, M. J., and Barderas, R. (2025) Deciphering the central role of TMOD2 in colorectal cancer progression and metastasis. *Br. J. Cancer*. https://doi.org/10.1038/s41416-025-03184-1
56. Sharma, V. P., Entenberg, D., and Condeelis, J. (2007) High-resolution live-cell imaging and time-lapse microscopy of invadopodium dynamics and tracking analysis. *Methods Mol. Biol.* **1046**, 343–358
57. Vannier, D. R., Shapeti, A., Chuffart, F., Planus, E., Manet, S., Rivier, P., *et al*. (2021) CCM2-deficient endothelial cells undergo a ROCK-dependent reprogramming into senescence-associated secretory phenotype. *Angiogenesis* **24**, 843–860
58. Murphy, R. (2018) On the use of one-sided statistical tests in biomedical research. *Clin. Exp. Pharmacol. Physiol.* **45**, 109–114
59. Lord, S. J., Velle, K. B., Dyche Mullins, R., and Fritz-Laylin, L. K. (2020) SuperPlots: communicating reproducibility and variability in cell biology. *J. Cell Biol.* https://doi.org/10.1083/JCB.202001064
60. Luque-García, J. L., Martínez-Torrecuadrada, J. L., Epifano, C., Cañamero, M., Babel, I., and Casal, J. I. (2010) Differential protein expression on the cell surface of colorectal cancer cells associated to tumor metastasis. *Proteomics* **10**, 940–952
61. Barderas, R., Mendes, M., Torres, S., Bartolomé, R. A., López-Lucendog, M., Villar-Vázquez, R., *et al*. (2013) In-depth characterization of the secretome of colorectal cancer metastatic cells identifies key proteins in cell adhesion, migration, and invasion. *Mol. Cell Proteomics* **12**, 1602–1620
62. Montero-Calle, A., Garranzo-Asensio, M., Poves, C., Sanz, R., Dziakova, J., Pelaez-Garcia, A., *et al*. (2024) In-Depth proteomic analysis of paraffin-embedded tissue samples from colorectal cancer patients revealed TXNDC17 and SLC8A1 as key proteins associated with the disease. *J. Proteome Res.* https://doi.org/10.1021/acs.jproteome.3c00749
63. Wang, K., Ning, S., Zhang, S., Jiang, M., Huang, Y., Pei, H., *et al*. (2025) Extracellular matrix stiffness regulates colorectal cancer progression via HSF4. *J. Exp. Clin. Cancer Res.* **44**, 1–21
64. Liu, Y., Beyer, A., and Aebersold, R. (2016) On the dependency of cellular protein levels on mRNA abundance. *Cell* **165**, 535–550
65. Vogel, C., and Marcotte, E. M. (2012) Insights into the regulation of protein abundance from proteomic and transcriptomic analyses. *Nat. Rev. Genet.* **13**, 227–232
66. Hoshino, A., Costa-Silva, B., Shen, T.-L., Rodrigues, G., Hashimoto, A., Mark, M. T., *et al*. (2015) Tumour exosome integrins determine organotropic metastasis. *Nature* **N527**, 329–335
67. Shimaoka, M., Kawamoto, E., Gaowa, A., Okamoto, T., and Park, E. J. (2019) Connexins and integrins in exosomes. *Cancers (Basel)* **11**. https://doi.org/10.3390/cancers11010106
68. Zhao, L., Ma, X., and Yu, J. (2021) Exosomes and organ-specific metastasis. *Mol. Ther. Methods Clin. Dev.* **22**, 133–147
69. Schwager, S. C., Bordeleau, F., Zhang, J., Antonyak, M. A., Cerione, R. A., and Reinhart-King, C. A. (2019) Matrix stiffness regulates microvesicle-induced fibroblast activation. *Am. J. Physiol. Cell Physiol.* **317**, C82–C92
70. Mahadik, P., and Patwardhan, S. (2023) ECM stiffness-regulated exosomal thrombospondin-1 promotes tunneling nanotubes-based cellular networking in breast cancer cells. *Arch. Biochem. Biophys.* **742**, 109624
71. Hanahan, D., and Weinberg, R. A. (2011) Hallmarks of cancer: the next generation. *Cell* **144**, 646–674
72. Friberg, S., and Nystrom, A. (2015) Cancer metastases: early dissemination and late recurrences. *Cancer Growth Metastasis* **8**, 43–49
73. Klein, C. A. (2020) Cancer progression and the invisible phase of metastatic colonization. *Nat. Rev. Cancer* **20**, 681–694
74. Hupfer, A., Brichkina, A., Koeniger, A., Keber, C., Denkert, C., Pfefferle, P., *et al*. (2021) Matrix stiffness drives stromal autophagy and promotes formation of a protumorigenic niche. *Proc. Natl. Acad. Sci. U. S. A.* **118**, 1–9
75. Yang, J., Celebi, L. E., Hawthorne, L., Ozcebe, S. G., and Zorlutuna, P. (2025) Substrate stiffness modulates fibroblast extracellular vesicle secretion via mechanotransduction pathways. *Small* **21**, e05261
76. Ting, L., Cowley, M. J., Hoon, S. L., Guilhaus, M., Raftery, M. J., and Cavicchioli, R. (2009) Normalization and statistical analysis of quantitative proteomics data generated by metabolic labeling. *Mol. Cell. Proteomics* **8**, 2227–2242

77. Kammers, K., Cole, R. N., Tiengwe, C., and Ruczinski, I. (2015) Detecting significant changes in protein abundance. *EuPA Open Proteomics* **7**, 11–19
78. Pursiheimo, A., Vehmas, A. P., Afzal, S., Suomi, T., Chand, T., Strauss, L., *et al*. (2015) Optimization of statistical methods impact on quantitative proteomics data. *J. Proteome Res.* **14**, 4118–4126
79. van Ooijen, M. P., Jong, V. L., Eijkemans, M. J. C., Heck, A. J. R., Andeweg, A. C., Binai, N. A., *et al*. (2018) Identification of differentially expressed peptides in high-throughput proteomics data. *Brief. Bioinform.* **19**, 971–981
80. Montero-Calle, A., López-Janeiro, Á., Mendes, M. L., Perez-Hernandez, D., Echevarría, I., Ruz-Caracuel, I., *et al*. (2023) In-depth quantitative proteomics analysis revealed C1GALT1 depletion in ECC-1 cells mimics an aggressive endometrial cancer phenotype observed in cancer patients with low C1GALT1 expression. *Cell. Oncol.* **46**, 697–715
81. Montero-Calle, A., Coronel, R., Garranzo-Asensio, M., Solís-Fernández, G., Rábano, A., de los Ríos, V., *et al*. (2023) Proteomics analysis of prefrontal cortex of Alzheimer's disease patients revealed dysregulated proteins in the disease and novel proteins associated with amyloid-β pathology. *Cell. Mol. Life Sci.* **80**, 1–26
82. Montero-Calle, A., Garranzo-Asensio, M., Rejas-González, R., Feliu, J., Mendiola, M., and Peláez-García, A. (2023) Benefits of FAIMS to improve the proteome coverage of deteriorated and/or cross-linked TMT 10-Plex FFPE tissue and plasma-derived exosomes samples. *Proteomes* **11**